Article

Cell Metabolism

Hepatocyte-Macrophage Acetoacetate Shuttle Protects against Tissue Fibrosis

Graphical Abstract

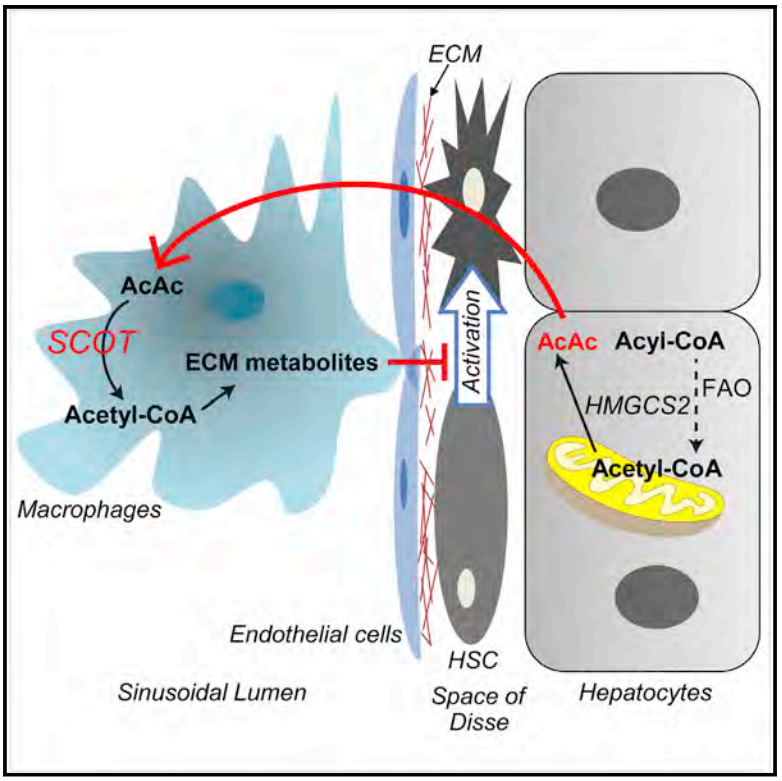

Authors

Patrycja Puchalska, Shannon E. Martin, Xiaojing Huang, ..., Laszlo Nagy, Gary J. Patti, Peter A. Crawford

Correspondence

crawforp@umn.edu

In Brief

Puchalska et al. combine stable isotope tracing with untargeted metabolomics to identify the specific roles of the ketone bodies, acetoacetate (AcAc) and D-β-hydroxybutyrate (D-βOHB), in mediating metabolic plasticity in macrophages. They unveil a hepatocyte-macrophage ketone shuttle and show that AcAc protects the liver from high-fat-diet-induced fibrosis.

Highlights

- Macrophages oxidize acetoacetate (AcAc), but not β-hydroxybutyrate
- Metabolism of AcAc in macrophages extends into pathways beyond the TCA cycle
- Effective AcAc competition with glucose requires its mitochondrial metabolism
- Mitochondrial AcAc metabolism in macrophages protects against liver fibrosis

Puchalska et al., 2019, Cell Metabolism *29*, 383–398
February 5, 2019
https://doi.org/10.1016/j.cmet.2018.10.015

CellPress

Cell Metabolism
Article

Hepatocyte-Macrophage Acetoacetate Shuttle Protects against Tissue Fibrosis

Patrycja Puchalska,[1,2] Shannon E. Martin,[2,3] Xiaojing Huang,[2,4,5] Justin E. Lengfeld,[1] Bence Daniel,[2,6] Mark J. Graham,[7] Xianlin Han,[2,8] Laszlo Nagy,[2,6,9] Gary J. Patti,[4] and Peter A. Crawford[1,2,10,11,*]

[1]Division of Molecular Medicine, Department of Medicine, University of Minnesota, 401 East River Parkway, MMC 194, Minneapolis, MN 55455, USA
[2]Center for Metabolic Origins of Disease, Sanford Burnham Prebys Medical Discovery Institute, Orlando, FL 32827, USA
[3]Pathobiology Graduate Program, Brown University, Providence, RI 02912, USA
[4]Department of Chemistry, Washington University, St. Louis, MO 63110, USA
[5]Department of Radiation Oncology, Memorial Sloan Kettering Cancer Center, New York, NY 10065, USA
[6]Department of Medicine, Johns Hopkins University School of Medicine, Johns Hopkins All Children's Hospital, Saint Petersburg, FL 33701, USA
[7]Ionis Pharmaceuticals, Carlsbad, CA 92010, USA
[8]Barshop Institute for Longevity and Aging Studies, Department of Medicine, Division of Diabetes, University of Texas Health Science Center at San Antonio, San Antonio, TX 78229, USA
[9]Department of Biological Chemistry, Johns Hopkins University School of Medicine, Johns Hopkins All Children's Hospital, Saint Petersburg, FL 33701, USA
[10]Department of Biochemistry, Molecular Biology, and Biophysics, University of Minnesota, Minneapolis, MN 55455, USA
[11]Lead Contact
*Correspondence: crawforp@umn.edu
https://doi.org/10.1016/j.cmet.2018.10.015

SUMMARY

Metabolic plasticity has been linked to polarized macrophage function, but mechanisms connecting specific fuels to tissue macrophage function remain unresolved. Here we apply a stable isotope tracing, mass spectrometry-based untargeted metabolomics approach to reveal the metabolome penetrated by hepatocyte-derived glucose and ketone bodies. In both classically and alternatively polarized macrophages, [^{13}C]acetoacetate (AcAc) labeled ~200 chemical features, but its reduced form D-[^{13}C]β-hydroxybutyrate (D-βOHB) labeled almost none. [^{13}C]glucose labeled ~500 features, and while unlabeled AcAc competed with only ~15% of them, the vast majority required the mitochondrial enzyme succinyl-coenzyme A-oxoacid transferase (SCOT). AcAc carbon labeled metabolites within the cytoplasmic glycosaminoglycan pathway, which regulates tissue fibrogenesis. Accordingly, livers of mice lacking SCOT in macrophages were predisposed to accelerated fibrogenesis. Exogenous AcAc, but not D-βOHB, ameliorated diet-induced hepatic fibrosis. These data support a hepatocyte-macrophage ketone shuttle that segregates AcAc from D-βOHB, coordinating the fibrogenic response to hepatic injury via mitochondrial metabolism in tissue macrophages.

INTRODUCTION

Ketone bodies are an alternative source of metabolic energy, especially during states of diminished carbohydrate availability (McGarry and Foster, 1980; Robinson and Williamson, 1980). Ketones are generated from fatty acid-derived acetyl-coenzyme A (CoA) through a series of reactions requiring the fate committing mitochondrial 3-hydroxymethylglutaryl (HMG)-CoA synthase (HMGCS2) expressed in hepatocytes and gut epithelial cells. Acetoacetate (AcAc) represents 25%–50% of the total ketone body pool produced by the liver, with the balance secreted as its reduced form D-β-hydroxybutyrate (D-βOHB), produced by mitochondrial D-βOHB dehydrogenase (BDH1) (Krebs and Hems, 1970; McGarry and Foster, 1971). Robust ketogenesis is relatively restricted to hepatocytes due to abundant HMGCS2 expression. After ketones are released from hepatocytes into the circulation, D-βOHB is oxidized to AcAc in mitochondria of extrahepatic cells via BDH1, and a CoA moiety is transferred from succinyl-CoA to AcAc via SCOT (succinyl-CoA-oxoacid transferase, encoded by the *Oxct1* gene), which prepares AcAc for terminal oxidation. SCOT's ubiquitous expression is excluded from hepatocytes, preventing ketone oxidation in these cells. While numerous metabolic pathways, such as β-oxidation, the tricarboxylic acid (TCA) cycle, and gluconeogenesis intersect with ketone body metabolism, the only known physiologically relevant metabolic fate of ketone bodies is their SCOT-dependent terminal oxidation in the TCA cycle. Multiple studies suggest diverse signaling roles for ketones, even in carbohydrate replete states, a subset of which could be independent of their metabolism (Puchalska and Crawford, 2017). For example, βOHB inhibits the NLRP3 inflammasome in macrophages and has neuroprotective effects on macrophages that may require signaling through the G protein coupled receptor GPR109A (Rahman et al., 2014; Youm et al., 2015).

Macrophage phenotypes in mammalian tissues exhibit marked metabolic plasticity, depending on cell ontogeny, tissue localization, and environmental stimuli (Puleston et al., 2017; Saha et al., 2017). Phenotypic features of classically polarized inflammatory (M1) and alternatively polarized reparative (M2)

macrophages helps to orient the wide spectrum of macrophage populations and functions (Kelly and O'Neill, 2015). The classically polarized phenotype is associated with tissue injury and inflammatory signaling and is triggered by pathogen-associated mediators such as lipopolysaccharides (LPSs) (Martinez and Gordon, 2014). The alternatively polarized phenotype antagonizes the inflammatory response, favoring tissue repair, remodeling, and fibrosis, and is triggered by activation of the IL-4/STAT6-dependent pathway (Minutti et al., 2017). Classically polarized macrophages employ glycolysis and the pentose phosphate pathway (PPP) to support microbicidal functions, whereas alternatively polarized macrophages leverage fatty acid oxidation for metabolic demands (Vats et al., 2006; Xu et al., 2015). Recent observations raise questions regarding the roles of metabolic fuels in macrophage function and whether all fuels are handled equivalently by polarized macrophages (Gonzalez-Hurtado et al., 2017; Nomura et al., 2016). Oxidation of alternative metabolic fuels such as ketones has been relatively unexplored in macrophages, although SCOT is abundantly expressed in bone marrow-derived macrophages (BMDMs) (Youm et al., 2015). To determine the roles of ketone body metabolism in macrophages, we developed a stable isotope tracing untargeted metabolomics (ITUM) pipeline utilizing liquid chromatography (LC)/high-accuracy mass spectrometry (MS). Until now, the utilization of stable isotopes has largely been confined either to differential distribution of label through known substrate-product relationships or to quantify canonical fluxes performed in stationary or non-stationary analysis. The convergence of stable isotope labels with untargeted metabolomics approaches until now has not been applied in disease-relevant contexts (also in Puchalska et al., 2018). We used cultured primary BMDMs to discover a set of mitochondrial and cytoplasmic metabolic pathways to which AcAc, but not βOHB, can contribute, many of which are shared with glucose-utilizing networks. Use of SCOT-deficient macrophages revealed mitochondrial metabolism as the predominant route. Loss of SCOT in hepatic tissue macrophages, lobular neighbors to ketone- and glucose-producing hepatocytes, predisposed mice to an exuberant fibrotic hepatic phenotype. These findings reveal a ketone shuttle between hepatocytes and local macrophages that modulates the liver's fibrotic response to increased fat ingestion and supports the notion that metabolism of the two ketone bodies AcAc and βOHB have segregated roles in macrophage biology.

RESULTS

Macrophages Oxidize AcAc, but Not βOHB

To study the metabolic fates of ketone bodies in macrophages, we cultured primary BMDMs and first confirmed phenotypic responses to stimulants of the classic (*Tnfa* gene, induced by LPS) and alternative (*Arg1* gene, induced by IL-4) polarization phenotypes (Figures S1A and S1B). To quantitatively determine the metabolic transformations of [^{13}C]AcAc or D-[^{13}C]βOHB in BMDMs, we applied ITUM, and analyzed the data with X^{13}CMS (Huang et al., 2014). This analytical platform sorts features (pairs of *m/z* and retention time) into isotopologue groups of putatively labeled metabolites and calculates the relative isotopic enrichment for each member. We tested ketone bodies at 1 mM, a concentration high enough to reveal cellular oxidation but still lower than achieved through starvation or ketogenic diets (Robinson and Williamson, 1980; Wildenhoff et al., 1974). After treatment for 6 or 24 hr of BMDM with 1 mM [U-$^{13}C_4$]AcAc, we observed up to 50% fractional ^{13}C enrichment of TCA cycle intermediates (Figures 1A, S1C, and S1D). Among polarized macrophage states, fractional ^{13}C enrichments of glutamate (a reporter of α-ketoglutarate) and malate were decreased by ~25% ($p < 0.001$) in LPS polarized macrophages, compared with unpolarized and IL-4-polarized BMDMs (Figure 1A). In contrast to AcAc, 1 mM D-[U-$^{13}C_4$]βOHB did not produce any ^{13}C labeling of TCA cycle intermediates in macrophages (Figure 1B), despite its avid uptake into these cells (Figure S1E). To become accessible for terminal oxidation, D-βOHB first requires NAD$^+$-dependent oxidation to AcAc by mitochondrial BDH1, whose ΔG favors D-βOHB formation, and is sensitive to the mitochondrial NAD$^+$/NADH ratio (Krebs et al., 1969; Williamson et al., 1967) (Figure 1C). While trace reduction to [^{13}C]βOHB was evident in extracts from [^{13}C]AcAc-treated BMDMs (Figure 1D), oxidation of [^{13}C]βOHB to [^{13}C]AcAc was undetectable (not shown). Accordingly, immunoblots revealed no observable BDH1 protein expression in BMDMs (Figure 1E). To confirm the absence of mitochondrial BDH activity in BMDMs, we increased the mitochondrial NAD$^+$/NADH ratio by treatment with the ionophore carbonyl cyanide-4-(trifluoromethoxy)phenylhydrazone (FCCP) (0.5–2 μM) for 6 hr. Under these conditions, which favor D-βOHB oxidation to AcAc, [^{13}C]βOHB also did not enrich TCA cycle pools (Figure 1F). Thus, irrespective of polarization state, BMDMs selectively oxidize AcAc but not D-βOHB. To the best of our knowledge, our data report for the first time impaired BDH1 expression in extrahepatic cells and selective utilization of ketone body redox partners.

AcAc Metabolism Converges with Non-oxidative Pathways in Macrophages

To determine whether macrophages allocate metabolites of [^{13}C]AcAc beyond TCA cycle intermediates, we used X^{13}CMS to interrogate datasets derived from BMDMs cultured in 1 mM [^{13}C]AcAc for 24 hr. The results were analyzed using the pipeline schematized in Figure 2A. In this approach, each labeled sample is compared with control unlabeled samples prepared under identical conditions, conferring datasets revealing increased abundances of ^{13}C isotopologues of identical metabolites, rather than increased abundances of alternative metabolites. We retrieved 187, 162, and 170 [^{13}C]AcAc-derived isotopologue groups for unpolarized, LPS-polarized, and IL-4-polarized macrophages, respectively (Table S1A). Mitochondrial acetyl-CoA can be exported to the cytosol as citrate through the citrate transporter (CIC)/ATP-citrate lyase system, which contributes to a multitude of pathways (Figure S1C). Indeed, intracellular substrate compartmentalization is highly polarization state dependent in macrophages (see also Puchalska et al., 2018). As observed for TCA cycle intermediates, D-[^{13}C]βOHB-derived ^{13}C labeling was negligible (Figure 2B; Table S1A).

To assign putative identities to the features labeled by [^{13}C]AcAc, we applied the PIUMet package (Pirhaji et al., 2016; see Table S1A for putative identification of all labeled features). PIUMet supported the putative identification of 68 metabolites in unpolarized macrophages, and 70 in each of the polarized (LPS or IL-4) macrophages (Figure S2A). Although the majority

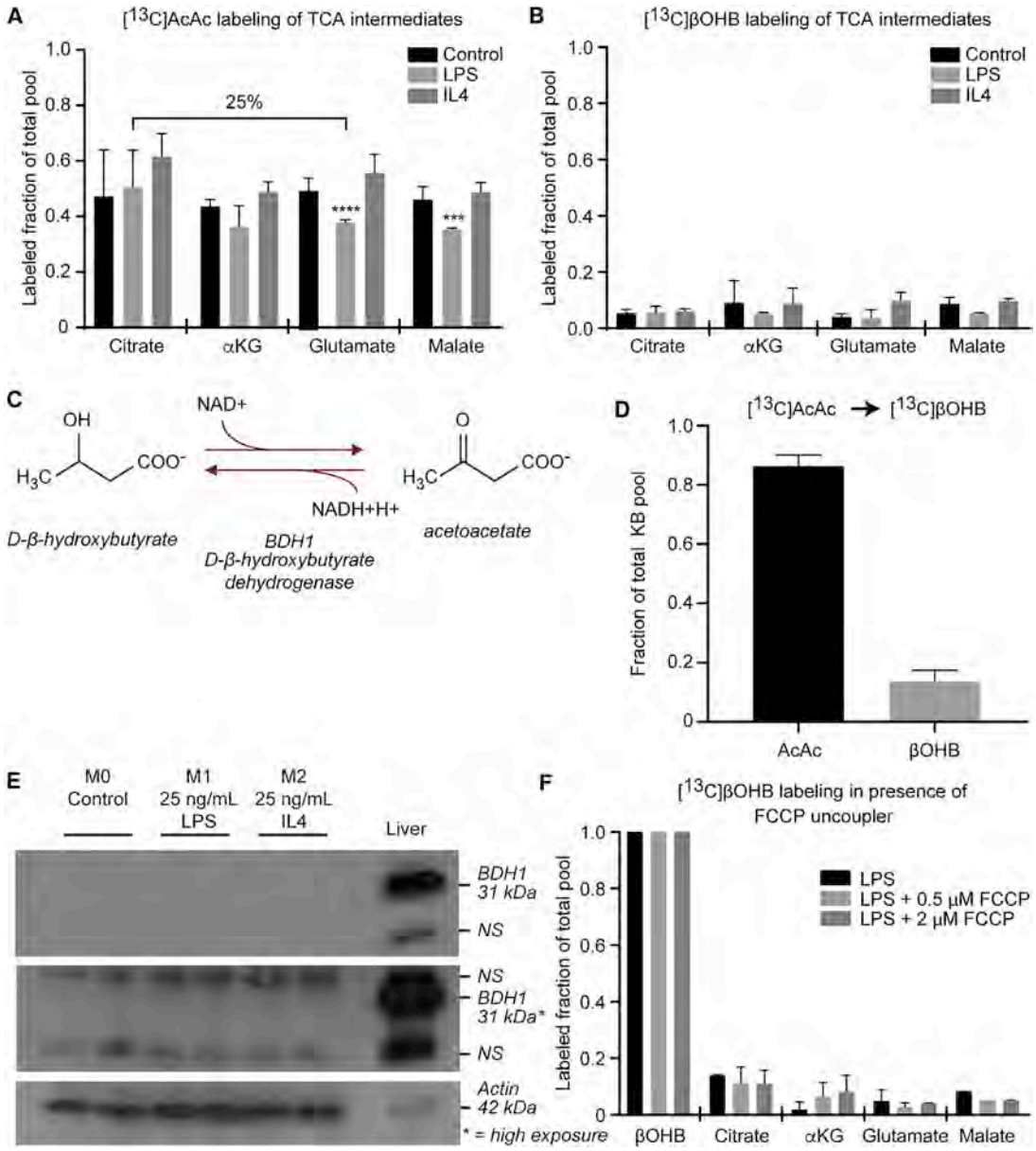

Figure 1. Oxidation of AcAc, but Not D-βOHB, by Primary BMDM

(A and B) (A) Labeling of TCA cycle intermediates with 1 mM [$^{13}C_4$]acetoacetate ([U-$^{13}C_4$]AcAc) or (B) D-[U-$^{13}C_4$]β-hydroxybutyrate (D-[$^{13}C_4$]βOHB) in unpolarized (control), LPS (25 ng/mL) or IL-4 (25 ng/mL) polarized WT BMDM after 24 hr of exposure (n > 3/group).

(C) Schematic of conversion of AcAc and D-βOHB by D-βOHB dehydrogenase 1 (BDH1).

(D) Fraction of total ketone body pool obtained from 1 mM [U-$^{13}C_4$]AcAc-treated macrophages (n = 12/group).

(E) Immunoblot for BDH1 protein, migrating at 31 kDa, and actin in protein BMDMs lysate after 24 hr of exposure (positive control: WT mouse liver). The center panel is a high exposure of upper panel blot. NS, non-specific signals.

(F) Labeling of TCA cycle intermediates in LPS polarized macrophages in the presence or absence of FCCP uncoupler (n = 2/group).

Data expressed as the mean ± SEM. Significant differences determined by multiple Student's t test with Holm-Sidak correction compared with control. ***p < 0.001; ****p < 0.0001; as indicated.

(45 identifications) of [^{13}C]AcAc-labeled metabolites were observed in all three macrophage states, the highest number (13 identifications) of uniquely labeled metabolites was observed in IL-4-polarized macrophages (Figure S2A). [^{13}C]AcAc-derived carbon was dispersed among amino acids, organic acids, nucleosides, nucleotides, and lipids (Figure 2C), indicating that AcAc is also directed into cytoplasmic and other cellular compartment pathways (Figure S2B). Mapping of [^{13}C]AcAc-derived putative metabolites into the KEGG (Kyoto Encyclopedia of Genes and Genomes) database revealed major contributions of AcAc-derived carbon into amino acid metabolism (Figure S2C; Table S1B). Thus, conversion of AcAc into acetyl-CoA opens fates

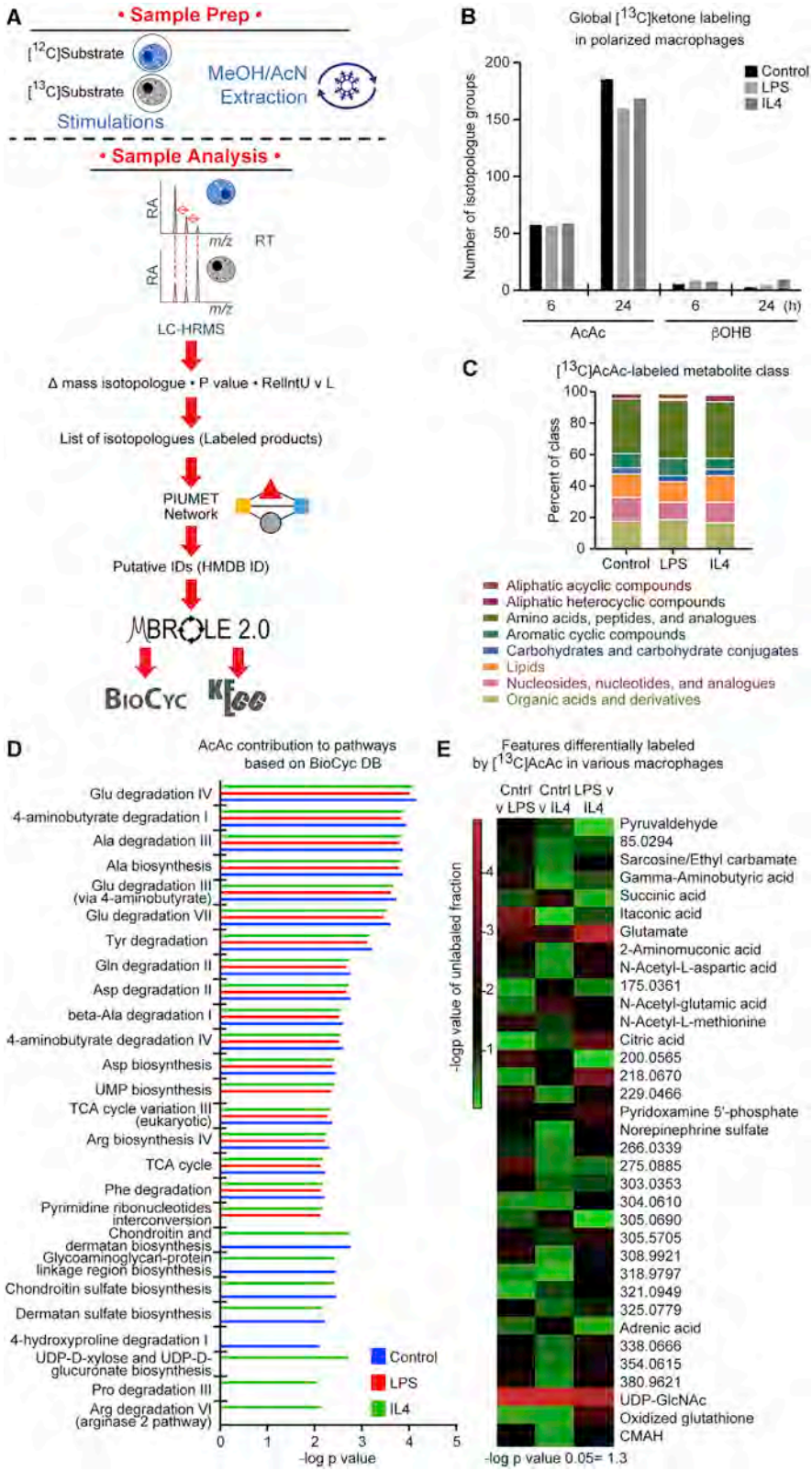

Figure 2. Incorporation of ^{13}C-Labeled AcAc into Non-oxidative Macrophage Pathways

(A) Schematic of stable isotope-based workflow applied in this study. ^{13}C-labeled and ^{12}C-unlabeled substrates are added to cells, which are extracted after incubation. Both extracts were analyzed on LC system linked to high-resolution MS (feature-pair of retention time [RT] and *m/z*). Based on the ion counts of

(legend continued on next page)

beyond TCA intermediates, many of which are metabolic precursors of these downstream products (Figure S1C).

Interrogation of [^{13}C]AcAc-labeled metabolites against the BioCyc database revealed, uniquely in IL-4-polarized macrophages, contribution of AcAc to putative glucuronide conjugates that mapped to the chondroitin sulfate (CS) and dermatan sulfate (DS) pathways, proline/arginine degradation, and uridine diphosphate (UDP)-biosynthetic pathways (Figure 2D). Selective labeling among macrophage states was evident for numerous features, including labeling of putative UDP N-acetylglucosamine (UDP-GlcNAc) (Figures 2B–2E; Table S1C). UDP-GlcNAc is the product of the hexosamine biosynthetic pathway (HBP), and the precursor of N-acetylneuraminic acid (NeuAc; a sialic acid), both of which contribute to the glycoprotein and/or glycosaminoglycan (GAG) pathways. However, the total labeled fraction varied among macrophage polarization states, suggesting polarization-dependent engagement of pathways connected to the HBP (see details in Puchalska et al., 2018). These data underscore that AcAc-derived carbon has fates beyond the TCA cycle in primary macrophages, with variations that depend on polarization state. Furthermore, the exclusive ability of [^{13}C]AcAc, but not its reduced form D-[^{13}C]βOHB, to contribute to both TCA intermediates and also a large repertoire of additional metabolites raises the hypothesis that mitochondria play a key role in the generation of these downstream cellular metabolites.

AcAc Successfully Competes with Glucose to Contribute to Diverse Metabolic Pathways in Alternatively Polarized Macrophages

As with most mammalian cells, tissue macrophages are simultaneously exposed to multiple substrates that can serve as carbon sources. To determine how macrophages coordinate the use of competing substrates, we first replaced glucose in BMDM culture medium with 10 mM [U-$^{13}C_6$]glucose. As expected (Xu et al., 2015), in LPS-polarized macrophages the relative abundances of the ^{13}C-labeled PPP intermediates were increased compared with unpolarized or IL-4-polarized states (Figure S3A). In contrast, labeling of downstream TCA intermediates in the LPS-polarized state was diminished by 29% for glutamate and 16% for malate ($p < 0.001$ and 0.01, respectively) (Figures S3B and S1C) similar to [^{13}C]AcAc labeling (Figure 1A). We then tested the ability of unlabeled 1 mM AcAc to compete with 10 mM [U-$^{13}C_6$]glucose. Because mitochondrial acetyl-CoA decreases glucose-derived pyruvate entry into the TCA cycle by inhibiting pyruvate dehydrogenase (PDH) (Figure S3C), we expected less incorporation of [^{13}C]glucose-derived acetyl-CoA into downstream metabolites in the presence of unlabeled AcAc (Cooper et al., 1975). Indeed, [^{13}C]glucose labeling of TCA intermediates in LPS- and IL-4-polarized macrophages was diminished 43%–60% and 33%–44% (all $p < 0.001$), respectively, in the presence of unlabeled AcAc (Figure 3A). These observations suggest preferential oxidation of AcAc over glucose in macrophages irrespective of their polarization state.

The metabolic conduit linking mitochondrial conversion of AcAc to acetyl-CoA, via SCOT⇒thiolase-dependent catalysis, to cytoplasmic metabolism is largely dependent on citrate export from mitochondria via the ATP-citrate lyase-dependent shuttle. However, cytosolic acetoacetyl-CoA synthetase (AACS) also supports the conversion of AcAc to acetyl-CoA (Edmond, 1974; Endemann et al., 1982). Therefore, we measured the expression of both *Aacs* and *Oxct1* genes in BMDMs and observed unique *Oxct1* induction 3-fold by IL-4 (Figure S4A). RNA sequencing (RNA-seq) analysis of IL-4-polarized BMDMs revealed a 5-fold increase of *Oxct1* mRNA 6 and 24 hr after IL-4 treatment, compared with control (Figures 3B and 3C). Accordingly, BMDMs harvested from STAT6 knockout mice (S6KO), which lack the transcription factor mediator downstream of IL-4 signaling, failed to increase *Oxct1* expression (Figure 3B) (Czimmerer et al., 2018; Kapoor et al., 2015). Analysis of STAT6-chromatin immunoprecipitation (ChIP) datasets revealed IL-4-dependent augmentation of STAT6 occupancy at −43 kb and −1.7 kb relative to the *Oxct1* transcription start site (Figure 3C) (Czimmerer et al., 2018). Thus, *Oxct1* is a potential STAT6 target in alternatively polarized macrophages, suggesting a dynamic role of mitochondrial ketone metabolism in this phenotypic state.

Given the potential role in alternatively polarized macrophages for SCOT, and thus AcAc metabolism, we focused our analysis on the fates of ^{13}C-labeled substrates in IL-4-polarized macrophages. [U-$^{13}C_6$]glucose labeled 249 features in both control and IL-4-polarized cells, with 63 of these exhibiting significant differences in label enrichment (Figure S4B). An additional 240 features were uniquely labeled by [U-$^{13}C_6$]glucose only in IL-4-polarized cells. Together, these 303 features were mapped to KEGG pathways, which confirmed increased labeling of TCA cycle, pyrimidine, arginine, proline, and purine pathways in alternatively polarized macrophages (Figure S4C). In IL-4-polarized macrophages, 71 out of the 446 (16%) features labeled by [U-$^{13}C_6$]glucose preferentially incorporated carbon derived from unlabeled AcAc (Figure 3D; Table S2). To reveal the cross-talk between mitochondrial-dependent ketone metabolism and glucose metabolism, we repeated substrate competition experiments in SCOT knockout (KO) IL-4-polarized macrophages. We confirmed loss of SCOT in BMDMs via immunoblot (Figure S4D) and demonstrated preserved canonical responses to LPS and IL-4 polarization in SCOT-KO BMDMs (Figure S4E). [^{13}C]AcAc was unable to label TCA intermediates in SCOT-KO BMDMs,

aligned features, the relative abundances (RAs) of each isotopologues in the group (signals within RT limits and the difference equal to 1.0034*n; n = number of ^{13}C) are calculated using X^{13}CMS. From the getIsoLabelReport the isotopologue groups are filtered based on the difference in mass of isotopologues, p values of enriched isotopologues (^{12}C versus ^{13}C conditions), and relative enrichment (RelIntUvL). List of isotopologues is subjected to PIUMET Network analysis and putative identifications are utilized for the pathway enrichment analysis against the *Mus musculus* KEGG and BioCyc databases.

(B) Numbers of labeled isotopologue groups from X^{13}CMS analysis indicating incorporation of ^{13}C label derived from either 1mM [U-$^{13}C_4$]AcAc or D-[U-$^{13}C_4$]βOHB in unpolarized (control), LPS (25 ng/mL), or IL-4 (25 ng/mL) polarized WT BMDMs after 6 or 24 hr of exposure (n = 3/group).

(C) Molecular structure-based classification of [$^{13}C_4$]AcAc-derived putative metabolite classes of WT BMDM after 24 hr of labeling (n = 3/group).

(D) Pathway enrichment analysis of 1 mM [U-$^{13}C_4$]AcAc-labeled putative metabolites based on BioCyc database in WT BMDMs.

(E) Heatmap of features differentially labeled by 1 mM [U-$^{13}C_4$]AcAc after 24 hr of treatment (p values from n = 3/group). Putative identifications assigned based on either PIUMET analysis or MS/MS (unassigned are depicted as *m/z*). The order on the heatmap is based on increasing *m/z* value.

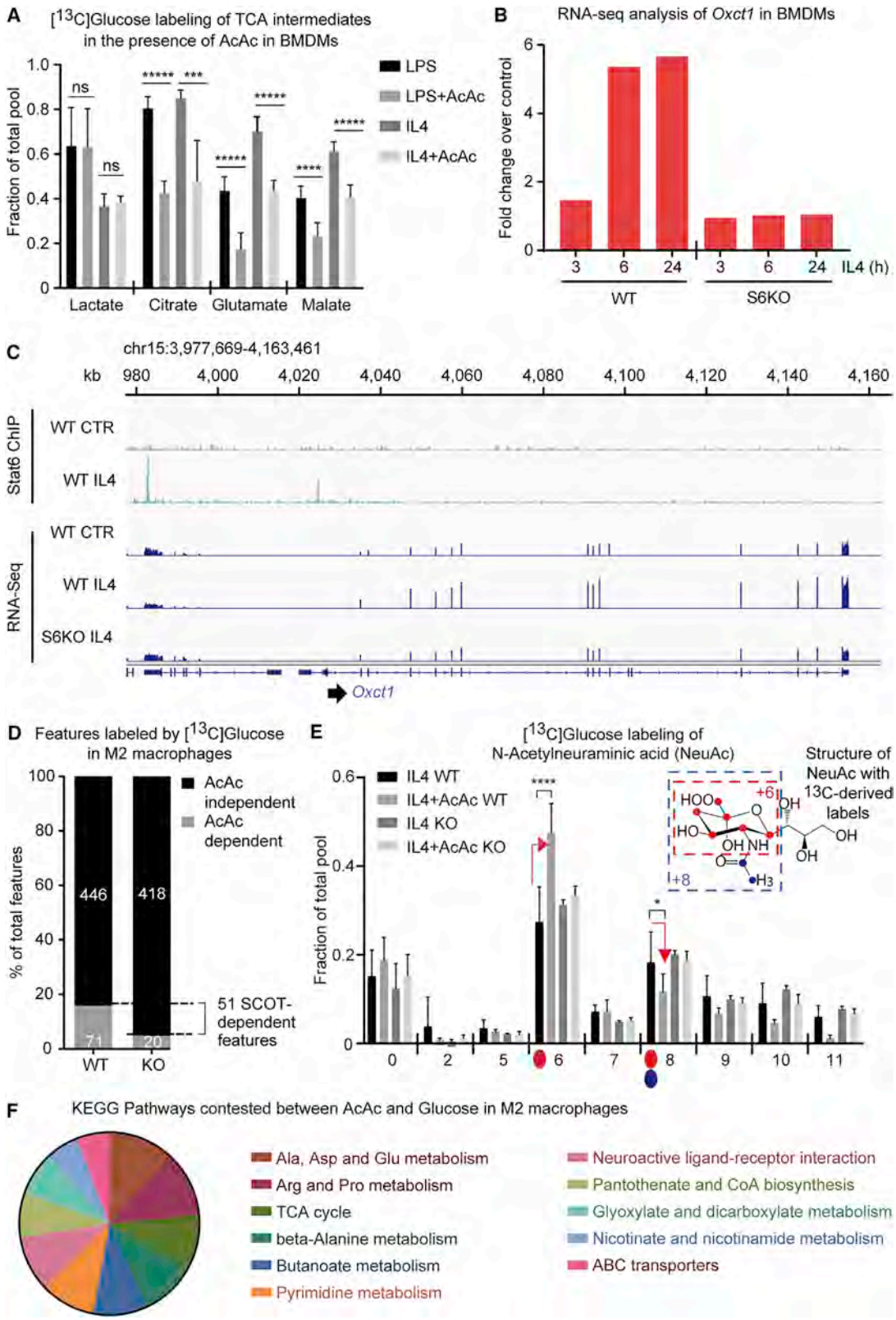

Figure 3. Mitochondrial Pathway Contributions of AcAc in Alternatively Polarized Macrophages

(A) Competition between 10 mM [U-$^{13}C_6$]glucose and 1 mM unlabeled AcAc carbons for TCA cycle intermediates in LPS (25 ng/mL) or IL-4 (25 ng/mL) polarized WT BMDMs after 24 hr of exposure (n > 7/group) (data utilized also in Puchalska et al., 2018).

(legend continued on next page)

while [^{13}C]glucose-derived labeling of TCA intermediates was normal (Figures S4F and S4G). Moreover, in IL-4-polarized SCOT-KO BMDMs, AcAc competed with [^{13}C]glucose-derived labeling of only 20 out of 418 glucose-labeled features, a 72% decrease compared with wild-type [WT] BMDMs ($p < 0.0001$ by Mann Whitney U test) (Figure 3D; Table S2), indicating a primary role of mitochondrial ketone metabolism in the context of mixed substrate exposure. To determine the requirement of mitochondrial AcAc metabolism in alternatively polarized macrophages, the 51 SCOT-dependent competed features were analyzed using PIUMet and MBRole pathway analysis (Tables S2 and S3), which revealed CS degradation (Figure S4H) similar to our [^{13}C]AcAc datasets (Figure 2D). One of the characteristic chemical features of this SCOT-dependent pathway was NeuAc (Figure 3E), a terminal sugar residue of glycan chains, which can be synthetized from UDP-GlcNAc (Figure S4I). Competition between AcAc and glucose for NeuAc labeling in WT IL-4-polarized BMDMs was abrogated in SCOT KO (Figure 3E). While mapping of the 51 SCOT-dependent [^{13}C]glucose-AcAc competing features to KEGG, the TCA cycle was a significant, but not major, contributor among the enriched pathways. Ala, Asp, Glu, Arg, and Pro metabolism (24% of SCOT-dependent features) contribute to the urea cycle, which includes the reaction catalyzed by the canonical alternatively polarized macrophage mediator arginase (Figure 3F; Table S3). Collectively, in the context of a physiological mix of substrate fuels, alternatively polarized macrophages leverage mitochondrial metabolism of AcAc to generate intermediates in multiple downstream metabolic pathways not directly linked to terminal oxidation.

Mitochondrial Ketone Metabolism in Macrophages Protects against Hepatic Fibrosis

The liver harbors one of the largest resident macrophage populations, Kupffer cells (Guilliams et al., 2016). Neighboring lobular hepatocytes release signals and metabolites, including glucose and ketone bodies, into the surrounding stroma. Ketogenesis occurs solely in hepatocytes, due to the abundant expression of mitochondrial HMGCS2, and, due to the absence of SCOT expression, hepatocytes do not oxidize the ketone bodies they generate (Orii et al., 2008). To determine the extent to which mitochondrial metabolism of AcAc supports homeostatic function of tissue macrophages *in vivo*, we generated macrophage-specific SCOT-KO mice using the LysM-Cre driver and maintained these mice and their littermate controls on a 60% kcal fat diet for 8 weeks (Figures 4A–4C). Administration of high-fat diet (HFD) for 8 weeks in WT mice causes hepatic steatosis and mild hepatocyte injury, necrosis, and lobular inflammation but typically does not cause fibrosis (Machado et al., 2015). SCOT-Macrophage-KO mice exhibited similar plasma total ketone body levels as littermate controls (Figure 4D), and blood glucose was increased 14% (Figure 4E; $p = 0.047$, $n > 10$/group) in SCOT-Macrophage-KO mice, although intraperitoneal glucose tolerance tests yielded similar excursions (Figure 4F). HFD-fed mice with loss of SCOT in macrophages maintain the same body weight as their littermates (Figure 4G), and liver steatosis was similar, as determined by oil red O staining (Figure 4H) and triacylglycerol quantification (Figure 4I). H&E stains of liver sections from SCOT-Macrophage-KO mice revealed comparable histological architecture to littermate controls (Figure 4J) and similar density of F4/80$^+$ macrophages (Figure S5A).

To reflect variations in hepatocyte-macrophage crosstalk through AcAc exchange, we acquired untargeted metabolomics data derived from liver extracts of SCOT-Macrophage-KO and littermate control mice. Analysis using XCMS online yielded 7,074 total features, of which 238 exhibited a statistically significant $\geq$2-fold change (Figure S5B; Table S4). Among the pathways with the most favorable p values ($p < 0.05$) were purine metabolism, histone degradation, UDP-GlcNAc/UDP-GalNAc biosynthesis, amino acid degradation, protein glycosylation, ketolysis, and DS degradation. Among the putative dysregulated metabolites was iduronate, whose total ion counts were downregulated 14% in livers of SCOT-Macrophage-KO mice ($p < 0.03$; Figure 5A). The identity of iduronate was corroborated using the Compound Discoverer package, which uses natural isotopic distribution to predict compound composition. While no direct relationship was evident between AcAc mitochondrial metabolism in macrophages and diminished static iduronate content in livers of SCOT-Macrophage-KO mice, L-iduronic acid (IdoA) is the major uronic acid within GAGs, and drew our attention due to preferential use of AcAc carbon to amino sugar and NeuAc GAG components within IL-4 polarized BMDMs (Figures 2D and 3E). Diverse GAGs, including CS/DS, are composed of polymers of varying amino sugar-uronic acid disaccharides, with varying degrees of sulfation. Macrophages exhibit increased GAG content upon IL-4 polarization, and perturbations in the GAG DS/CS pathways are associated with expansion of extracellular matrix (ECM) that lead to the development of hepatic fibrosis (Decaris et al., 2017; Habuchi et al., 2016; Martinez et al., 2015). Thus, we next asked if metabolic perturbations of GAG metabolism observed both in cultured macrophages lacking SCOT and liver tissue from animals lacking SCOT in macrophages were linked to hepatic fibrogenesis.

Transcriptional signatures of altered fibrogenesis were evident in livers of SCOT-Macrophage-KO mice, with upregulation of the

(B and C) RNA-seq (B) and ChIP sequencing (C) analysis of *Oxct1* (encodes SCOT) in WT and STAT6 knockout (S6KO) BMDMs exposed to IL-4 (20 ng/mL) for the indicated period of time. Gene expression values are in fragments per kilobase of exon per million fragments mapped format. Fold change over vehicle-treated cells is presented for each time point.

(D) Number of features contested between 10 mM [U-$^{13}C_6$]glucose and 1 mM unlabeled AcAc in IL-4 polarized WT and SCOT-KO BMDMs after 24 hr of treatment (n = 4/group).

(E) 10 mM [$^{13}C_6$]glucose labeling of N-acetyl-neuraminic acid (NeuAc) from intact glucose (red dots) and an acetyl group (blue dots) in IL-4 (25 ng/mL) polarized WT and SCOT-KO BMDM after 24 hr of exposure (n = 4/group). Labeling of the acetyl group derived from mitochondrial acetyl-CoA production from [U-$^{13}C_6$] glucose-derived pyruvate (M+8 isotopologue, labeled glucose, and acetyl group) or from 1mM [^{12}C]AcAc, which decreases the M+8 isotopologue, and increases the M+6 isotopologue. Pattern was abrogated in SCOT-KO BMDMs.

(F) Distribution of glucose-ketone competing putative metabolites into KEGG pathways in IL-4 polarized BMDMs.

Data expressed as mean ± SEM. Significant differences determined by multiple Student's t test with Holm-Sidak correction compared with unpolarized control or by two-way ANOVA. *$p < 0.05$; ***$p < 0.001$; ****$p < 0.0001$; *****$p < 0.00001$; as indicated.

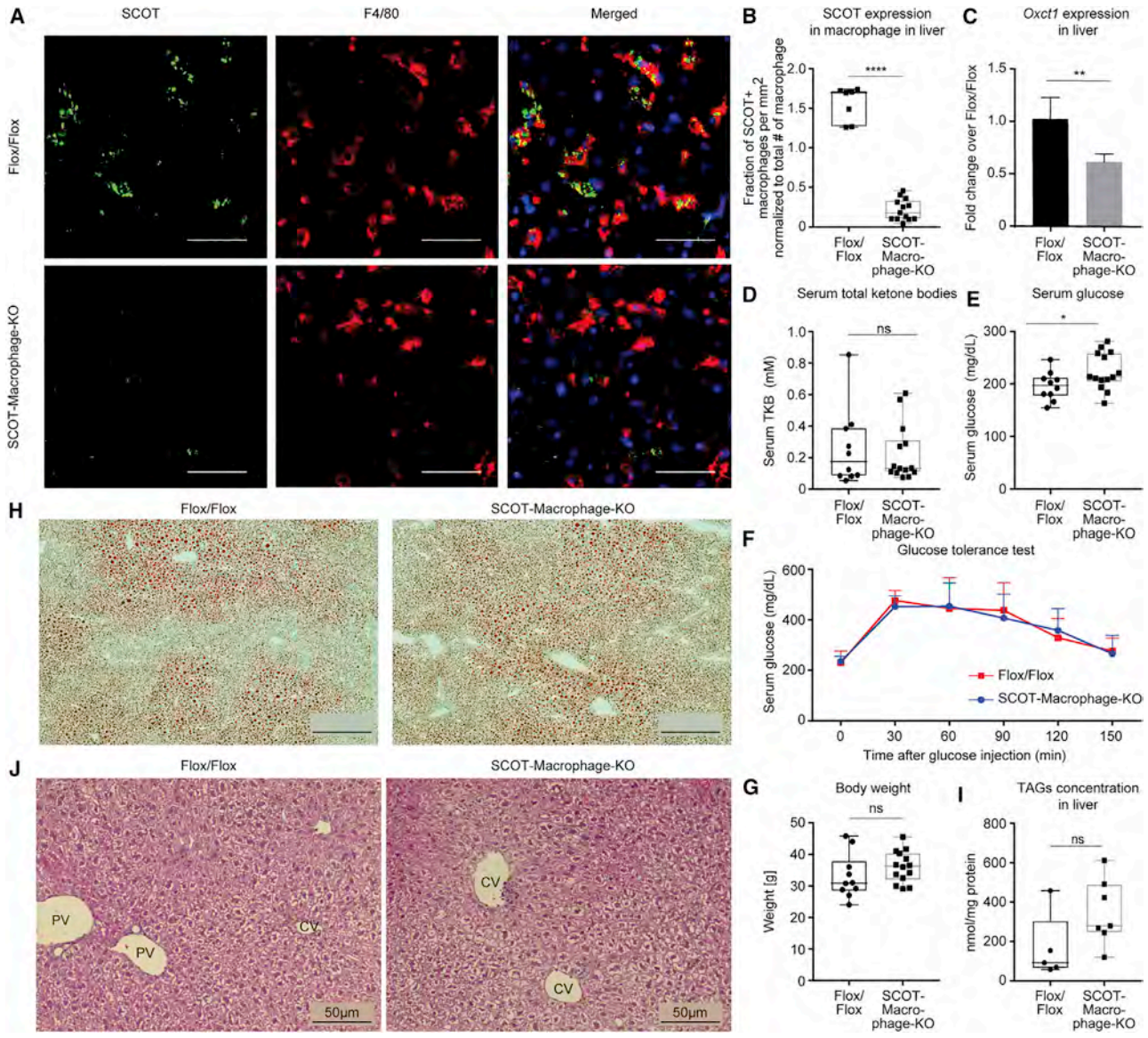

Figure 4. SCOT-Macrophage-KO Mice Exhibit Normal Physiological Responses to HFD

(A and B) (A) Representative 20× magnification of immunohistochemical stains for SCOT and F4/80^{+} (DAPI labeling of cellular nuclei, blue), and (B) relative number of SCOT-positive macrophages in cryosections of livers from *Oxct1*$^{flox/flox}$ controls (Flox/Flox) and SCOT-Macrophage-KO mice fed HFD for 8 weeks (n > 7/group). (C) *Oxct1* gene expression in livers (n > 4/group).

(D–G) (D) Serum total ketone bodies (TKBs) concentration (mM) (n > 10/group), (E) blood glucose concentration (mg/dL) (n > 10/group; p = 0.0471), (F) intraperitoneal glucose tolerance test (n = 4/group), and (G) body weight (g) (n > 10/group) of *Oxct1*$^{flox/flox}$ (Flox/Flox) control and SCOT-Macrophage-KO mice.

(H–J) (H) Representative oil red O staining of liver sections together with (I) quantification of hepatic triacylglycerol (TAG) concentration (nmol/mg protein) (n > 5/group; p = 0.093), and (J) H&E staining of liver sections from *Oxct1*$^{flox/flox}$ control (Flox/Flox) and SCOT-Macrophage-KO (scale bar, 50 μm). CV, central vein. PV, portal vein.

Data expressed as the mean ± SEM. Significant differences determined by Student's t test. *p < 0.05; **p < 0.01; ****p < 0.0001; as indicated.

mRNAs for angiogenic factor *Vegfc* (vascular endothelial growth factor C), mitogen *Pdgfa* (platelet-derived growth factor A), profibrotic cytokine *Il13*, and a marker of monocyte recruitment *Cd11b* (Figure 5B). Mediators of immune cell recruitment upon liver injury (*Ccl3*, *Ccl5*, *Loxl1*) were also significantly upregulated in livers of SCOT-Macrophage-KO mice (Figure 5C), together with *Ym1* and *Fizz1* genes, canonical markers of M2 polarization (Figure 5D). *Arg1* mRNA was unchanged due to the presence in both macrophages and hepatocytes (Figure S5C). *Tgfb* (transforming growth factor β), inflammatory cytokines (*Tnfa*, *Il1b*, and *Il6*), and oxidative stress markers (*Nos2*, *Hmox1*, and *Nrf2*) were unchanged in livers of SCOT-Macrophage-KO mice (Figure S5C). However, markers of hepatic stellate cell activation and trans-differentiation into myofibroblasts (*Shh*, *Igfbp5*, *Acta2*) were elevated, suggesting that hepatic stellate cells may also be a target of hepatocyte-derived AcAc (Figure 5C).

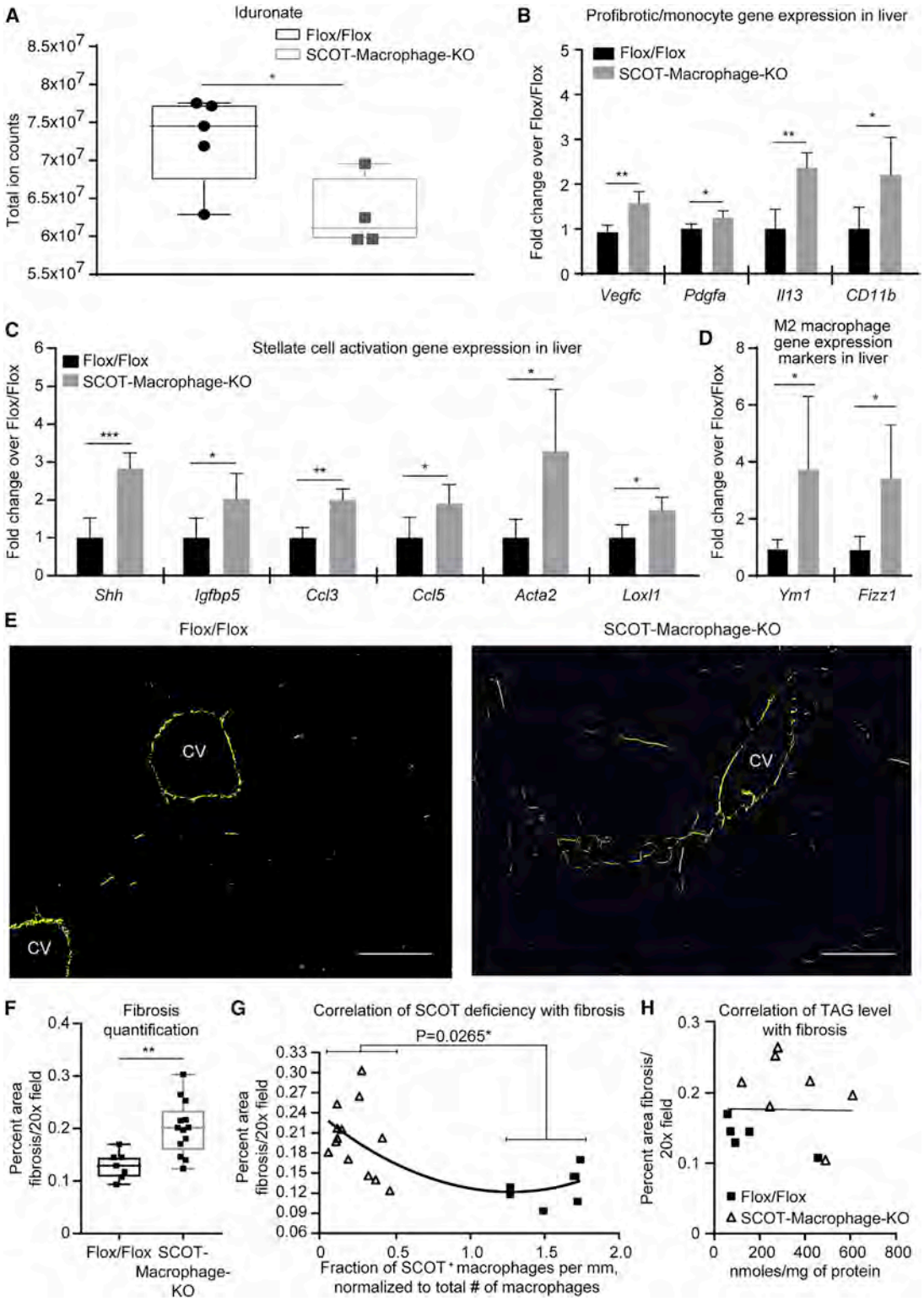

Figure 5. Loss of SCOT in Hepatic Tissue Macrophages Is Associated with an Accelerated Fibrotic Response to HFD

(A) Total ion counts of putative iduronate (*m/z* = 193.0354) obtained from untargeted LC/MS analysis of *Oxct1*$^{flox/flox}$ control (Flox/Flox) and SCOT-Macrophage-KO livers (n = 4–5/group).

(B–D) (B) Transcript abundances of profibrotic, monocyte recruitment, (C) hepatic stellate cell activation biomarkers, and (D) M2 polarized macrophage markers genes in *Oxct1*$^{flox/flox}$ control (Flox/Flox) and SCOT-Macrophage-KO mice fed HFD for 8 weeks (n > 4/group). *Vegfc*, vascular endothelial growth factor C; *Pdgfa*, platelet-derived growth factor A; *Il13*, interleukin 13; *Cd11b*, integrin subunit alpha M; *Shh*, Sonic Hedgehog; *Igfbp5*, insulin-like growth factor binding protein 3;

(legend continued on next page)

Because a proportion of hepatic stellate cells may derive from hematopoietic progenitors (Miyata et al., 2008) and be susceptible to Cre-mediated recombination in the LysM-Cre model, we performed anti-desmin/anti-SCOT double-labeling confocal immunohistochemistry in livers obtained from HFD-fed control and SCOT-Macrophage-KO mice. Abundant desmin/SCOT double-positive cells persisted in SCOT-Macrophage-KO livers (Figure S5D), suggesting that stellate cell phenotypes in SCOT-Macrophage-KO mice are downstream of loss of SCOT in LysM-Cre$^+$ cells. Phenotypes observed in livers of SCOT-Macrophage-KO mice are likely restricted to hepatic macrophages, as adipokines and inflammatory mediators exhibited normal expression in subcutaneous (inguinal) adipose tissue (Figures S5E and S5F).

Consistent with the metabolomics and gene expression datasets, picrosirius red stains showed a 55% increase ($p < 0.006$, $n > 7$ animals/group, 20 fields analyzed/animal) in the total fibrotic area compared with littermate controls (Figures 5E and 5F). The magnitude of fibrosis correlated inversely with the fraction of SCOT$^+$/F4/80$^+$ macrophages, normalized to all F4/80$^+$ macrophages present in the tissue sections ($r^2 = 0.4623$, $p = 0.03$) (Figure 5G) but had no relationship to the magnitude of steatosis ($r^2 = 0.0001$) (Figure 5H). To confirm the role of locally derived ketogenesis from neighboring hepatocytes, we quantified fibrogenesis in ketogenesis-insufficient mice that are unable to produce ketones in liver (*Hmgcs2*-targeted antisense oligonucleotides [ASO]) and maintained these mice on HFD for 8 weeks (Cotter et al., 2014). These mice fail to express HMGCS2 protein in liver, while gut HMGCS2 protein is preserved, and, irrespective of the presence of SCOT in macrophages, these mice exhibited hypoketonemia in the random fed state (Figures S6A–S6C). Untargeted metabolomics studies of livers of ketogenesis-insufficient mice revealed 1,306 features dysregulated >2-fold compared with livers of controls (Figure 6A; Table S4). Putative features corresponding to iduronate were altered in livers of ketogenesis-insufficient animals, indicating perturbation of the DS/CS pathway (Table S4; Figure S6D). Indeed, *Hmgcs2* ASO treatment increased susceptibility to hepatic injury to HFD and increased inflammation and evidence of activated stellate cells (Cotter et al., 2014). Strikingly, livers of *Hmgcs2* ASO-treated animals that also lacked SCOT selectively in macrophages exhibited exuberant inflammation, hepatocyte injury, and profound degradation of hepatic lobular structure (Figures 6B and 6C). Picrosirius red staining revealed increased fibrosis in livers of mice lacking both hepatocyte HMGCS2 and macrophage SCOT (Figures 6C and 6D). In summary, ketogenic insufficiency increased lobular fibrosis in both WT and SCOT-Macrophage-KO mice, and loss of SCOT in macrophages predisposed to hepatic fibrosis, independent of *Hmgcs2* ASO treatment (>50% increase in fibrosis in both ketogenesis-sufficient and -insufficient states; $p < 0.05$ for each comparison; Figures 6B–6D).

To determine whether exogenously administered AcAc recapitulates an anti-fibrotic effect, we maintained WT mice on a fibrogenic diet composed of *trans* fat, fructose, and cholesterol for 4 weeks (Soufi et al., 2014). During the fibrogenic interval, either AcAc (10 μmol/g body weight), D-βOHB (10 μmol/g body weight), or vehicle controls were administered every 12 hr via intraperitoneal (i.p.) injections. Pilot kinetic analyses indicated that ketones are completely metabolized within 15 min (AcAc more rapidly than D-βOHB) (Figure S7A). No significant changes in caloric consumption were observed between ketone-injected groups (Figure S7B), and body weights were comparable among groups (Figure S7C). Blood glucose concentrations at the end of the fibrogenic interval were not altered by ketone injections (Figure S7D). Because *in vitro* synthesis of AcAc generates equimolar ethanol, an equivalent ethanol concentration was used as vehicle, and saline was used as a vehicle for D-βOHB. Each dose (AcAc or vehicle) corresponded to <0.5 g ethanol/kg body weight, far below doses used to induce alcoholic hepatitis, and were not associated with systemic signs of toxicity, compared with saline control-treated animals (Gao et al., 2017). At the end of study, picrosirius red staining of liver sections from AcAc-treated animals showed a 52% reduction of hepatic fibrosis compared with vehicle control animals fed the fibrogenic diet ($p = 0.004$, $n = 7$/group; Figures 6E and 6G). Consistent with the divergent metabolic response of cultured primary BMDMs to the two ketone bodies, liver sections from mice injected with D-βOHB exhibited modestly augmented fibrosis in comparison with control animals (Figures 6F and S7E). It is possible that low-concentration ethanol dosing enhances the toxic effects of the fibrogenic diet (comparing the two different vehicle groups; Figures 6E and 6F). Nonetheless, the added presence of AcAc to this vehicle was protective. These results strongly support the contention that mitochondrial macrophage metabolism of either locally produced or systemically administered AcAc, but not D-βOHB, attenuates the hepatic fibrogenic response triggered by elevated nutritional fat.

DISCUSSION

The studies presented herein reveal two primary conclusions. First, an AcAc shuttle released from hepatocytes to neighboring macrophages transduces a mitochondrial metabolism-dependent signal that protects against hepatic lobular fibrogenesis in response to HFD. Second, βOHB is restricted from this shuttle because it cannot be metabolized by macrophage mitochondria. Both findings were generated through the ITUM platform, in which stable isotope tracing analysis was fully untargeted. Multiple analyses revealed a strong molecular metabolite candidate

Acta2, smooth muscle actin; *Ccl3*, C-C motif chemokine ligand 3; *Ccl5*, C-C motif chemokine ligand 5; *Loxl1*, lysyl oxidase like 1; *Fizz1*, resistin-like beta; *Ym1*, chitinase-like 3.

(E and F) (E) Representative 20× magnification of picrosirius red-stained liver sections together with (F) quantification (% area/20× field) from *Oxct1*$^{flox/flox}$ control (Flox/Flox) and SCOT-Macrophage-KO mice ($n > 7$/group).

(G and H) (G) Correlation between hepatic fibrosis level and relative number of SCOT-positive macrophages (20 correlation points) or (H) total TAG pools (nmoles/protein) in livers of *Oxct1*$^{flox/flox}$ control (Flox/Flox), and SCOT-Macrophage-KO mice maintained on HFD for 8 weeks.

Data expressed as the mean ± SEM. Significant differences determined by Student's t test. Correlation determined by fitting within polynomial (second order) or linear regression. *$p < 0.05$; **$p < 0.01$; ***$p < 0.001$; as indicated.

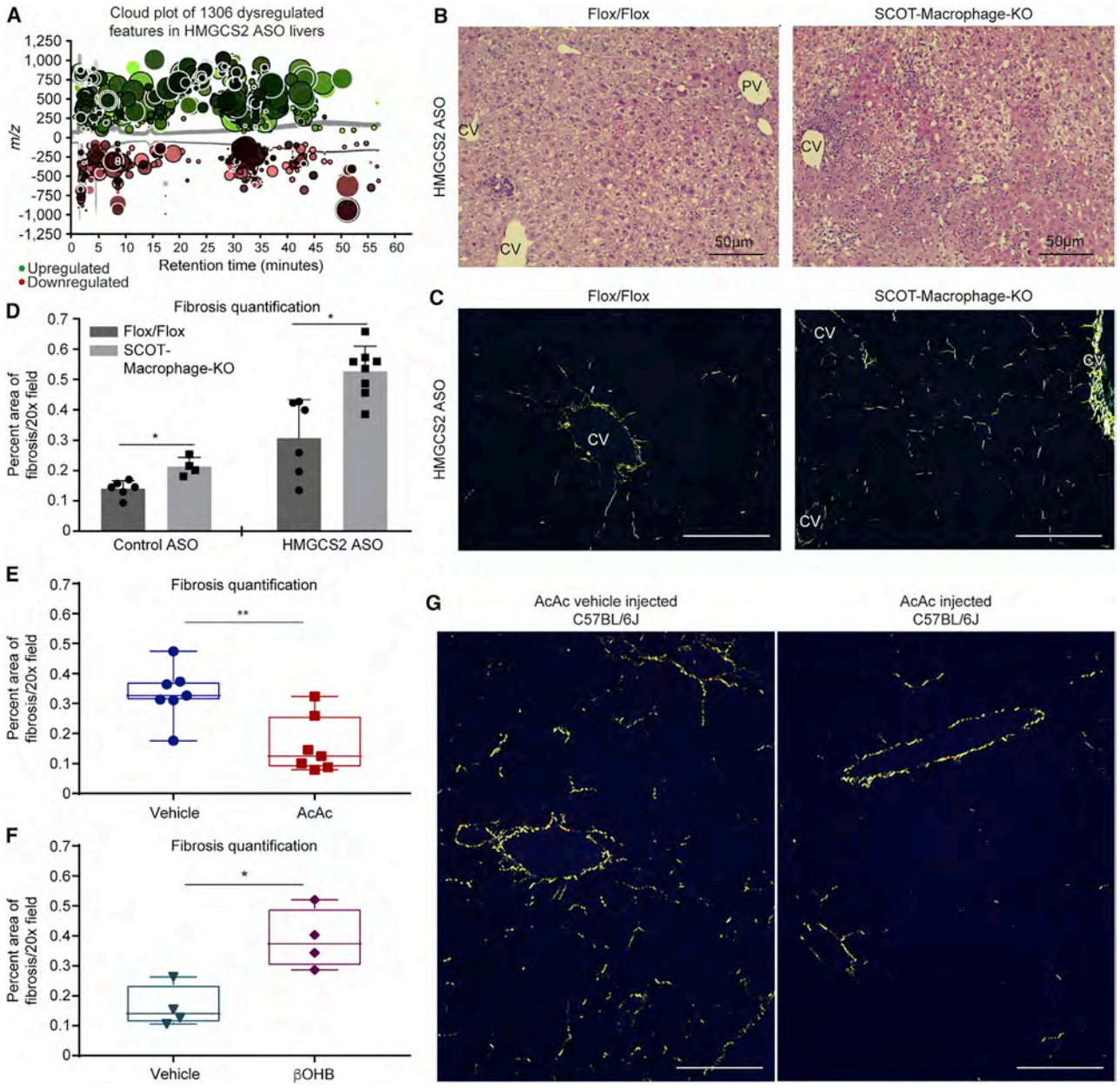

Figure 6. Hepatocyte Ketogenesis and Tissue Macrophage Mitochondrial Ketone Metabolism Independently and Additively Coordinate the Hepatic Fibrotic Response in Mice

(A) XCMS online cloud plot of 1,306 dysregulated chemical features when comparing antisense oligonucleotide (ASO)-treated control and *Hmgcs2* ASO (ketogenesis insufficient) livers (n = 4/group) of mice maintained on HFD for 8 weeks. The radius represents the fold change of upregulated (green) and downregulated (red) features, compared to control ASO, whereas shading depicts proportion to p value.

(B and C) (B) Representative H&E (scale bar, 50 μm) and (C) picrosirius red staining of liver sections from *Hmgcs2* ASO-treated mice on the *Oxct1*$^{flox/flox}$ control (Flox/Flox) and SCOT-Macrophage-KO backgrounds maintained on HFD for 8 weeks.

(D–F) (D) Quantification of picrosirius red-positive area (% area/20× field) in ASO-treated mice on *Oxct1*$^{flox/flox}$ control (Flox/Flox) and SCOT-Macrophage-KO backgrounds (n > 6/group). Quantification of picrosirius red-positive stain area (% area/20× field) in WT mice maintained on high-fat fibrogenic diet and injected with (E) AcAc (n = 7/group) or (F) D-βOHB (n = 4/group) and their representative vehicles (ethanol for AcAc and NaCl for D-βOHB) twice a day with 10 μmol/g body weight each for 4 weeks.

(G) Representative picrosirius red stains of liver sections obtained from the AcAc and its vehicle groups.

Data expressed as mean ± SEM. Significant differences determined by Student's t test or ANOVA with multiple comparisons with Tukey post-hoc tests, as appropriate. *p < 0.05; **p < 0.01; as indicated.

as a potential conduit for AcAc carbon in alternatively polarized macrophages, the GAGs. Indeed, revelation of macrophage GAG metabolism stimulated the hypothesis that a hepatocyte-macrophage AcAc shuttle regulates hepatic lobular fibrosis, which was further supported by genetic mouse models. A protective effect of AcAc was observed in animals in the energy-replete fed state and did not require provocation by fasting-induced ketogenesis, while exogenous AcAc (and not βOHB) was also protective from diet-induced hepatic lobular fibrosis. Thus, analogous to the lactate shuttle posed in the CNS, or the branched chain amino acid metabolite 3-hydroxyisobutyrate in muscle, liver is a highly plausible organ in which a local AcAc shuttle could exist (Brooks, 2018; Jang et al., 2016; Liu et al., 2017b). Our observations also indicate that substrate fuel selection, availability, and partitioning directly influence polarized macrophage function (Saha et al., 2017; Verdeguer and Aouadi, 2017).

While the observations herein are consistent with the benefits of nutritionally provoked ketogenesis in both human and animal models of nonalcoholic fatty liver disease (NAFLD)/nonalcoholic steatohepatitis (NASH), they indicate that independent effects of AcAc versus βOHB may influence the benefits of ketosis (Mardinoglu et al., 2018; Pawlak et al., 2015). Independent effects of ketones are important to consider due to physiological variations in the AcAc/βOHB ratio secreted by the liver (Krebs and Hems, 1970; McGarry and Foster, 1971). Responses to individual ketone bodies may vary and depend on target cell type and ketogenic rate (Puchalska and Crawford, 2017). Indeed, βOHB has been linked to anti-inflammatory responses in macrophages (Rahman et al., 2014; Youm et al., 2015), while AcAc can promote inflammatory signaling and oxidative stress (Jain et al., 2002; Kanikarla-Marie and Jain, 2015; Kurepa et al., 2012). Macrophages integrate numerous signals, and intact βOHB macrophage signaling could explain the lack of inflammation in fibrogenic livers of SCOT-Macrophage-KO mice, while superimposed HMGCS2 deficiency (which limits, but does not eliminate ketogenesis; Cotter et al., 2014; d'Avignon et al., 2018) yields both inflammation and fibrosis. However, recurrent boluses of high D-βOHB concentrations may provoke toxic responses in non-macrophages. Indeed, high-concentration βOHB activates pro-inflammatory and oxidative stress in calf hepatocytes and in other cell types (Meroni et al., 2018; Shi et al., 2014). Thus, tissue responses to ketone bodies require attentiveness to (1) distinct cell type responses within a tissue; (2) the delivered AcAc/βOHB ratio (including, but not limited to, mitochondrial redox potential effect); (3) total ketone body concentration and kinetics; and (4) augmenting or competing signals. Exogenous ketone preparations for prospective therapeutic or health-maintaining ends, including ketone esters, requires diligent attention to all of these principles.

While AcAc contributes to sterol and fatty acid biosynthesis through cytosolic AACS in extrahepatic cell types, the contribution of AcAc through mitochondrial (SCOT-dependent) routes to cytosolic pathways has not been previously demonstrated (Hasegawa et al., 2012; Yamasaki et al., 2016). Here (and in Puchalska et al., 2018) we demonstrate that AcAc-derived carbon, in an SCOT-dependent manner, contributes to GAG/glycoprotein/proteoglycan canonical metabolic pathways via labeling of UDP-GlcNAc/GalNAc or NeuAc in macrophages. Indeed, substrate selection and downstream metabolism may be equally important to support anabolic pathways and provide covalent modifiers for post-translational modifications, rather than fulfilling obligate cellular energy requirements (Schoors et al., 2015; Wong et al., 2017).

The composition of GAGs/ECM is remodeled under diet-induced metabolic disorders, hypercholesterolemia, diabetes, and cirrhosis, and while exogenous administration of purified GAGs ameliorates inflammation, oxidative stress, and fibrogenesis, decreases in GAG synthesis are fibrogenic (Campo et al., 2004; Liu et al., 2017a). The cellular component of GAGs is remodeled during monocyte-macrophage differentiation and depends on polarization (Chang et al., 2012; Martinez et al., 2015). While the primary drivers of ECM expansion and fibrosis in liver are hepatic stellate cells, macrophages produce proteoglycans (i.e., protein-GAG complexes) and ECM-modifying enzymes that may configure the fibrogenic cascade (Laskin et al., 1991; Matsubayashi et al., 2017; Winberg et al., 2000). GAG species may exert opposing actions on tissue fibrogenesis, with some exerting inhibitory roles in tissue fibrosis (Chen and Birk, 2013; Vogel et al., 1984). These results support a model in which hepatocyte-derived AcAc represents a safe signal to neighboring macrophages in a manner that is critical for GAG homeostasis in the fed state.

Hepatic fibrosis develops in response to numerous insults, including persistent overnutrition, genetic abnormalities of lipid metabolism, viral infection, toxins, ethanol, and autoimmune reactions, all of which lead to chronic immune activation that results in excessive production of ECM (Diehl and Day, 2017; Koyama and Brenner, 2017). Additionally, stimuli derived from injured hepatocytes, tissue macrophages, and/or endothelial cells activate hepatic stellate cells and promote their differentiation to myofibroblasts (Friedman, 2008; Pellicoro et al., 2014). Inflammation-independent hepatic fibrosis has been observed in select circumstances (e.g., hemochromatosis), and thus, while inflammation is a key trigger, it is not absolutely required to induce a fibrogenic cascade. While the mRNA encoding TGFβ was not augmented in our studies, it is possible that metabolic cues sensed by tissue macrophages operate through downstream mechanisms. Indeed, we observed activation of stellate cell, angiogenic factors, mediators of hedgehog pathway, and metabolomics signals consistent with cell proliferation, amino acid degradation, protein glycosylation, the HBP, and DS/CS synthesis.

Metabolic and histopathological features influenced by hepatic tissue macrophages could represent the effects on resident and/or recruited macrophages, as myeloid cells throughout the body lack SCOT in the LysM-Cre-driven SCOT-Macrophage-KO model. Resident (fetal liver/yolk sac-derived, F4/80^{Hi}Cd11b$^{Lo/Int}$) macrophages in the liver (Kupffer cells) may indeed harbor important functional differences compared with recruited BMDMs (F4/80$^{Lo/Int}$/Cd11b^{Hi}) (Mowat et al., 2017). Commonly in NAFLD progression to NASH, inflammation is mediated by recruited macrophages, while Kupffer cells exhibit an anti-inflammatory alternatively polarized phenotype, though bone marrow monocytes can generate self-renewing and fully differentiated Kupffer cells (Koyama and Brenner, 2017; Scott et al., 2016). Although hematopoiesis-derived LysM-Cre^{+}/desmin^{-} fibrocytes may directly contribute to the fibrogenic

hepatic myofibroblast population, the contributing fractions remain incompletely understood, and non-hematopoietic (LysM-Cre$^-$/desmin$^+$) trans-differentiated hepatic stellate cells are likely the primarily fibrogenic myofibroblast population (Mederacke et al., 2013; Xu and Kisseleva, 2015). The likelihood that an AcAc shuttle's coordination of hepatic fibrogenesis signals first through lobular macrophages is supported by a lack of phenotype in adipose tissue of SCOT-Macrophage-KO mice. Thus, extrahepatic alteration of myeloid cells and/or secretion of adipokines are likely not significant contributors to hepatic fibrogenesis in the SCOT-Macrophage-KO mice model (Adolph et al., 2017). Finally, the presence of abundant desmin$^+$/SCOT$^+$ cells in livers of fibrogenic SCOT-Macrophage-KO mice suggests that the effects of AcAc on these effector cells are first modulated through local LysM-Cre$^+$ cells. Thus, although trans-differentiation of hepatic stellate cells is probably promoted by Kupffer cell macrophages that lack SCOT, future studies need to segregate the roles of mitochondrial ketone metabolism among cell types, and also between AcAc versus D-βOHB among different immune and fibrosis effectors in steatohepatitis amelioration. Due to the highly conserved wound-healing process leading to fibrogenesis (Dobie et al., 2015; Pellicoro et al., 2014), our observations in the liver may be relevant in other organs, although the liver is especially poised to leverage ketones due to their abundant production in neighboring hepatocytes, even in the fed state.

Limitations of Study

ITUM highlights the contribution of hepatocyte-derived AcAc into diverse macrophage metabolic pathways beyond the TCA cycle, including the GAG cytosolic synthetic pathway. Quantitative measures of AcAc's dynamic influence over substrate-product relationships in the turnover of diverse GAG species in hepatic macrophages, and in liver tissue, remain to be determined. In addition, future studies will resolve quantitative shifts in GAG species diversity and the associated impact on hepatic fibrogenesis.

STAR★METHODS

Detailed methods are provided in the online version of this paper and include the following:

- KEY RESOURCES TABLE
- CONTACT FOR REAGENT AND RESOURCE SHARING
- EXPERIMENTAL MODEL AND SUBJECT DETAILS
  - Animal Models and Animal Model for Primary Cells
  - Bone Marrow- Derived Macrophage (BMDM) Isolation and Culture
- METHOD DETAILS
  - Synthesis of AcAc
  - Exogenous Delivery of Ketone Bodies
  - Labeling of Cultured Primary Cells by Stable Isotopes
  - Extraction of Metabolites from Cells, Liver Tissue and Conditioned Media
  - Targeted and Untargeted LC/MS Analysis
  - LC/MS Data Processing
  - Identification of Metabolites Detected in LC/MS and Pathway Analysis
  - Gene Expression Analysis
  - Immunoblotting
  - Histology and Immunohistochemical Staining
  - RNA-Seq and Analysis
  - ChIP-Seq (Chromatin Immunoprecipitation Followed by Sequencing) and Analysis
  - Shotgun Lipidomics-Guided TAG Quantification
  - Serum Ketone Body, Glucose Assays and Glucose Tolerance Test (GTT)
- QUANTIFICATION AND STATISTICAL ANALYSIS
- DATA AND SOFTWARE AVAILABILITY

SUPPLEMENTAL INFORMATION

Supplemental Information includes seven figures and five tables and can be found with this article online at https://doi.org/10.1016/j.cmet.2018.10.015.

ACKNOWLEDGMENTS

The authors thank J. Matthew Gandy and Matthew Longo for mouse husbandry, Peter E. Phelan for guidance on primary macrophage isolation and culture, and Laura Kyro for graphics expertise. This work was supported in part by grants from the NIH (DK091538, DK115924, CA235482, ES028365, and OD024624). B.D. is supported by the American Heart Association (AHA) postdoctoral fellowship (17POST33660450).

AUTHOR CONTRIBUTIONS

Conceptualization, P.P., X. Huang, and P.A.C.; Methodology, P.P., S.E.M., X. Huang, J.E.L., B.D., L.N., M.J.G., X. Han, G.J.P., and P.A.C.; Investigation, P.P., S.E.M., X. Huang, J.E.L., and B.D.; Resources, P.A.C. and M.J.G.; Writing – Original Draft, P.P. and P.A.C.; Writing – Review & Editing, all authors; Visualization, P.P., X. Huang, J.E.L., B.D., and P.A.C.; Supervision, X. Han, L.N., G.J.P., and P.A.C.; Funding Acquisition, P.A.C.

DECLARATION OF INTERESTS

M.J.G. is an employee and shareholder of Ionis Pharmaceuticals.

Received: February 21, 2018
Revised: August 20, 2018
Accepted: October 24, 2018
Published: November 15, 2018

SUPPORTING CITATIONS

The following reference appears in the Supplemental Information: Booth et al. (2013).

REFERENCES

Adolph, T.E., Grander, C., Grabherr, F., and Tilg, H. (2017). Adipokines and non-alcoholic fatty liver disease: multiple interactions. Int. J. Mol. Sci. *18*, https://doi.org/10.3390/ijms18081649.

Barta, E. (2011). Command line analysis of ChIP-seq results. EMBnet J. *17*, 13–17.

Booth, S.C., Weljie, A.M., and Turner, R.J. (2013). Computational tools for the secondary analysis of metabolomics experiments. Comput. Struct. Biotechnol. J. *4*, e201301003.

Brooks, G.A. (2018). The science and translation of lactate shuttle theory. Cell Metab. *27*, 757–785.

Campo, G.M., Avenoso, A., Campo, S., Ferlazzo, A.M., Micali, C., Zanghi, L., and Calatroni, A. (2004). Hyaluronic acid and chondroitin-4-sulphate treatment reduces damage in carbon tetrachloride-induced acute rat liver injury. Life Sci. *74*, 1289–1305.

Chang, M.Y., Chan, C.K., Braun, K.R., Green, P.S., O'Brien, K.D., Chait, A., Day, A.J., and Wight, T.N. (2012). Monocyte-to-macrophage differentiation: synthesis and secretion of a complex extracellular matrix. J. Biol. Chem. *287*, 14122–14135.

Chen, S., and Birk, D.E. (2013). The regulatory roles of small leucine-rich proteoglycans in extracellular matrix assembly. FEBS J. *280*, 2120–2137.

Chen, Y.J., Mahieu, N.G., Huang, X., Singh, M., Crawford, P.A., Johnson, S.L., Gross, R.W., Schaefer, J., and Patti, G.J. (2016). Lactate metabolism is associated with mammalian mitochondria. Nat. Chem. Biol. *12*, 937–943.

Cooper, R.H., Randle, P.J., and Denton, R.M. (1975). Stimulation of phosphorylation and inactivation of pyruvate dehydrogenase by physiological inhibitors of the pyruvate dehydrogenase reaction. Nature *257*, 808–809.

Cotter, D.G., Ercal, B., Huang, X., Leid, J.M., d'Avignon, D.A., Graham, M.J., Dietzen, D.J., Brunt, E.M., Patti, G.J., and Crawford, P.A. (2014). Ketogenesis prevents diet-induced fatty liver injury and hyperglycemia. J. Clin. Invest. *124*, 5175–5190.

Cotter, D.G., Schugar, R.C., Wentz, A.E., d'Avignon, D.A., and Crawford, P.A. (2013). Successful adaptation to ketosis by mice with tissue-specific deficiency of ketone body oxidation. Am. J. Physiol. Endocrinol. Metab. *304*, E363–E374.

Czimmerer, Z., Daniel, B., Horvath, A., Rückerl, D., Nagy, G., Kiss, M., Peloquin, M., Budai, M.M., Cuaranta-Monroy, I., Simandi, Z., et al. (2018). The transcription factor STAT6 mediates direct repression of inflammatory enhancers and limits activation of alternatively polarized macrophages. Immunity *48*, 75–90.e6.

Daniel, B., Balint, B.L., Nagy, Z.S., and Nagy, L. (2014a). Mapping the genomic binding sites of the activated retinoid X receptor in murine bone marrow-derived macrophages using chromatin immunoprecipitation sequencing. Methods Mol. Biol. *1204*, 15–24.

Daniel, B., Nagy, G., Hah, N., Horvath, A., Czimmerer, Z., Poliska, S., Gyuris, T., Keirsse, J., Gysemans, C., Van Ginderachter, J.A., et al. (2014b). The active enhancer network operated by liganded RXR supports angiogenic activity in macrophages. Genes Dev. *28*, 1562–1577.

d'Avignon, D.A., Puchalska, P., Ercal, B., Chang, Y., Martin, S.E., Graham, M.J., Patti, G.J., Han, X., and Crawford, P.A. (2018). Hepatic ketogenic insufficiency reprograms hepatic glycogen metabolism and the lipidome. JCI Insight *3*, e99762.

Decaris, M.L., Li, K.W., Emson, C.L., Gatmaitan, M., Liu, S., Wang, Y., Nyangau, E., Colangelo, M., Angel, T.E., Beysen, C., et al. (2017). Identifying nonalcoholic fatty liver disease patients with active fibrosis by measuring extracellular matrix remodeling rates in tissue and blood. Hepatology *65*, 78–88.

Diehl, A.M., and Day, C. (2017). Cause, pathogenesis, and treatment of nonalcoholic steatohepatitis. N. Engl. J. Med. *377*, 2063–2072.

Dobie, R., Connelly, J., and Henderson, N.C. (2015). PDGF-mediated regulation of liver fibrosis. Curr. Pathobiol. Rep. *3*, 225–233.

Edmond, J. (1974). Ketone bodies as precursors of sterols and fatty acids in the developing rat. J. Biol. Chem. *249*, 72–80.

Endemann, G., Goetz, P.G., Edmond, J., and Brunengraber, H. (1982). Lipogenesis from ketone bodies in the isolated perfused rat liver. Evidence for the cytosolic activation of acetoacetate. J. Biol. Chem. *257*, 3434–3440.

Friedman, S.L. (2008). Hepatic stellate cells: protean, multifunctional, and enigmatic cells of the liver. Physiol. Rev. *88*, 125–172.

Garbow, J.R., Doherty, J.M., Schugar, R.C., Travers, S., Weber, M.L., Wentz, A.E., Ezenwajiaku, N., Cotter, D.G., Brunt, E.M., and Crawford, P.A. (2011). Hepatic steatosis, inflammation, and ER stress in mice maintained long term on a very low-carbohydrate ketogenic diet. Am. J. Physiol. Gastrointest. Liver Physiol. *300*, G956–G967.

Gao, B., Xu, M.J., Bertola, A., Wang, H., Zhou, Z., and Liangpunsakul, S. (2017). Animal models of alcoholic liver disease: pathogenesis and clinical relevance. Gene Expr. *17*, 173–186.

Gonzalez-Hurtado, E., Lee, J., Choi, J., Selen Alpergin, E.S., Collins, S.L., Horton, M.R., and Wolfgang, M.J. (2017). The loss of macrophage fatty acid oxidation does not potentiate systemic metabolic dysfunction. Am. J. Physiol. Endocrinol. Metab. *312*, E381–E393.

Guilliams, M., Dutertre, C.A., Scott, C.L., McGovern, N., Sichien, D., Chakarov, S., Van Gassen, S., Chen, J., Poidinger, M., De Prijck, S., et al. (2016). Unsupervised high-dimensional analysis aligns dendritic cells across tissues and species. Immunity *45*, 669–684.

Habuchi, H., Ushida, T., and Habuchi, O. (2016). Mice deficient in N-acetylgalactosamine 4-sulfate 6-O-sulfotransferase exhibit enhanced liver fibrosis and delayed recovery from fibrosis in carbon tetrachloride-treated mice. Heliyon *2*, e00138.

Han, X., Yang, J., Cheng, H., Ye, H., and Gross, R.W. (2004). Toward fingerprinting cellular lipidomes directly from biological samples by two-dimensional electrospray ionization mass spectrometry. Anal. Biochem. *330*, 317–331.

Hasegawa, S., Ikeda, Y., Yamasaki, M., and Fukui, T. (2012). The role of acetoacetyl-CoA synthetase, a ketone body-utilizing enzyme, in 3T3-L1 adipocyte differentiation. Biol. Pharm. Bull. *35*, 1980–1985.

Huang, X., Chen, Y.J., Cho, K., Nikolskiy, I., Crawford, P.A., and Patti, G.J. (2014). X13CMS: global tracking of isotopic labels in untargeted metabolomics. Anal. Chem. *86*, 1632–1639.

Jain, S.K., Kannan, K., Lim, G., McVie, R., and Bocchini, J.A., Jr. (2002). Hyperketonemia increases tumor necrosis factor-alpha secretion in cultured U937 monocytes and type 1 diabetic patients and is apparently mediated by oxidative stress and cAMP deficiency. Diabetes *51*, 2287–2293.

Jang, C., Oh, S.F., Wada, S., Rowe, G.C., Liu, L., Chan, M.C., Rhee, J., Hoshino, A., Kim, B., Ibrahim, A., et al. (2016). A branched-chain amino acid metabolite drives vascular fatty acid transport and causes insulin resistance. Nat. Med. *22*, 421–426.

Kanikarla-Marie, P., and Jain, S.K. (2015). Hyperketonemia (acetoacetate) upregulates NADPH oxidase 4 and elevates oxidative stress, ICAM-1, and monocyte adhesivity in endothelial cells. Cell. Physiol. Biochem. *35*, 364–373.

Kapoor, N., Niu, J., Saad, Y., Kumar, S., Sirakova, T., Becerra, E., Li, X., and Kolattukudy, P.E. (2015). Transcription factors STAT6 and KLF4 implement macrophage polarization via the dual catalytic powers of MCPIP. J. Immunol. *194*, 6011–6023.

Kelly, B., and O'Neill, L.A. (2015). Metabolic reprogramming in macrophages and dendritic cells in innate immunity. Cell Res. *25*, 771–784.

Koyama, Y., and Brenner, D.A. (2017). Liver inflammation and fibrosis. J. Clin. Invest. *127*, 55–64.

Krebs, H.A., and Hems, R. (1970). Fatty acid metabolism in the perfused rat liver. Biochem. J. *119*, 525–533.

Krebs, H.A., Wallace, P.G., Hems, R., and Freedland, R.A. (1969). Rates of ketone-body formation in the perfused rat liver. Biochem. J. *112*, 595–600.

Kurepa, D., Pramanik, A.K., Kakkilaya, V., Caldito, G., Groome, L.J., Bocchini, J.A., and Jain, S.K. (2012). Elevated acetoacetate and monocyte chemotactic protein-1 levels in cord blood of infants of diabetic mothers. Neonatology *102*, 163–168.

Laskin, J.D., Dokidis, A., Gardner, C.R., and Laskin, D.L. (1991). Changes in sulfated proteoglycan production after activation of rat liver macrophages. Hepatology *14*, 306–312.

Liu, C.H., Lan, C.T., Chou, J.F., Tseng, T.J., and Liao, W.C. (2017a). CHSY1 promotes aggressive phenotypes of hepatocellular carcinoma cells via activation of the hedgehog signaling pathway. Cancer Lett. *403*, 280–288.

Liu, L., MacKenzie, K.R., Putluri, N., Maletić-Savatić, M., and Bellen, H.J. (2017b). The glia-neuron lactate shuttle and elevated ROS promote lipid synthesis in neurons and lipid droplet accumulation in glia via APOE/D. Cell Metab. *26*, 719–737.

Lopez-Ibanez, J., Pazos, F., and Chagoyen, M. (2016). MBROLE 2.0-functional enrichment of chemical compounds. Nucleic Acids Res. *44*, W201–W204.

Machado, M.V., Michelotti, G.A., Xie, G., Almeida Pereira, T., Boursier, J., Bohnic, B., Guy, C.D., and Diehl, A.M. (2015). Mouse models of diet-induced

nonalcoholic steatohepatitis reproduce the heterogeneity of the human disease. PLoS One *10*, e0127991.

Mahieu, N.G., Spalding, J.L., and Patti, G.J. (2016a). Warpgroup: increased precision of metabolomic data processing by consensus integration bound analysis. Bioinformatics *32*, 268–275.

Mahieu, N.G., Genenbacher, J.L., and Patti, G.J. (2016b). A roadmap for the XCMS family of software solutions in metabolomics. Curr. Opin. Chem. Biol. *30*, 87–93.

Mardinoglu, A., Wu, H., Bjornson, E., Zhang, C., Hakkarainen, A., Rasanen, S.M., Lee, S., Mancina, R.M., Bergentall, M., Pietilainen, K.H., et al. (2018). An integrated understanding of the rapid metabolic benefits of a carbohydrate-restricted diet on hepatic steatosis in humans. Cell Metab. *27*, 559–571.

Martinez, F.O., and Gordon, S. (2014). The M1 and M2 paradigm of macrophage activation: time for reassessment. F1000prime Rep. *6*, 13, eCollection 2014.

Martinez, P., Denys, A., Delos, M., Sikora, A.S., Carpentier, M., Julien, S., Pestel, J., and Allain, F. (2015). Macrophage polarization alters the expression and sulfation pattern of glycosaminoglycans. Glycobiology *25*, 502–513.

Matsubayashi, Y., Louani, A., Dragu, A., Sanchez-Sanchez, B.J., Serna-Morales, E., Yolland, L., Gyoergy, A., Vizcay, G., Fleck, R.A., Heddleston, J.M., et al. (2017). A moving source of matrix components is essential for de novo basement membrane formation. Curr. Biol. *27*, 3526–3534.e4.

McGarry, J.D., and Foster, D.W. (1980). Regulation of hepatic fatty acid oxidation and ketone body production. Annu. Rev. Biochem. *49*, 395–420.

McGarry, J.D., and Foster, D.W. (1971). The regulation of ketogenesis from octanoic acid. The role of the tricarboxylic acid cycle and fatty acid synthesis. J. Biol. Chem. *246*, 1149–1159.

Mederacke, I., Hsu, C.C., Troeger, J.S., Huebener, P., Mu, X., Dapito, D.H., Pradere, J.P., and Schwabe, R.F. (2013). Fate tracing reveals hepatic stellate cells as dominant contributors to liver fibrosis independent of its aetiology. Nat. Commun. *4*, 2823.

Meroni, E., Papini, N., Criscuoli, F., Casiraghi, M.C., Massaccesi, L., Basilico, N., and Erba, D. (2018). Metabolic responses in endothelial cells following exposure to ketone bodies. Nutrients *10*, E250.

Minutti, C.M., Knipper, J.A., Allen, J.E., and Zaiss, D.M.W. (2017). Tissue-specific contribution of macrophages to wound healing. Semin. Cell Dev. Biol. *61*, 3–11.

Miyata, E., Masuya, M., Yoshida, S., Nakamura, S., Kato, K., Sugimoto, Y., Shibasaki, T., Yamamura, K., Ohishi, K., Nishii, K., et al. (2008). Hematopoietic origin of hepatic stellate cells in the adult liver. Blood *111*, 2427–2435.

Mowat, A.M., Scott, C.L., and Bain, C.C. (2017). Barrier-tissue macrophages: functional adaptation to environmental challenges. Nat. Med. *23*, 1258–1270.

Nomura, M., Liu, J., Rovira, I.I., Gonzalez-Hurtado, E., Lee, J., Wolfgang, M.J., and Finkel, T. (2016). Fatty acid oxidation in macrophage polarization. Nat. Immunol. *17*, 216–217.

Orii, K.E., Fukao, T., Song, X.Q., Mitchell, G.A., and Kondo, N. (2008). Liver-specific silencing of the human gene encoding succinyl-CoA: 3-ketoacid CoA transferase. Tohoku J. Exp. Med. *215*, 227–236.

Pawlak, M., Baugé, E., Lalloyer, F., Lefebvre, P., and Staels, B. (2015). Ketone body therapy protects from lipotoxicity and acute liver failure upon Pparα deficiency. Mol. Endocrinol. *29*, 1134–1143.

Pellicoro, A., Ramachandran, P., Iredale, J.P., and Fallowfield, J.A. (2014). Liver fibrosis and repair: immune regulation of wound healing in a solid organ. Nat. Rev. Immunol. *14*, 181–194.

Pirhaji, L., Milani, P., Leidl, M., Curran, T., Avila-Pacheco, J., Clish, C.B., White, F.M., Saghatelian, A., and Fraenkel, E. (2016). Revealing disease-associated pathways by network integration of untargeted metabolomics. Nat. Methods *13*, 770–776.

Puchalska, P., Huang, X., Martin, S., Han, X., Patti, G., and Crawford, P. (2018). Isotope tracing untargeted metabolomics reveals macrophage polarization state-specific metabolic coordination across intracellular compartments. iScience. Published online November 2, 2018. https://doi.org/10.1016/j.isci.2018.10.029.

Puchalska, P., and Crawford, P.A. (2017). Multi-dimensional roles of ketone bodies in fuel metabolism, signaling, and therapeutics. Cell Metab. *25*, 262–284.

Puleston, D.J., Villa, M., and Pearce, E.L. (2017). Ancillary activity: beyond core metabolism in immune cells. Cell Metab. *26*, 131–141.

Rahman, M., Muhammad, S., Khan, M.A., Chen, H., Ridder, D.A., Muller-Fielitz, H., Pokorna, B., Vollbrandt, T., Stolting, I., Nadrowitz, R., et al. (2014). The B-hydroxybutyrate receptor HCA2 activates a neuroprotective subset of macrophages. Nat. Commun. *5*, 3944.

Robinson, A.M., and Williamson, D.H. (1980). Physiological roles of ketone bodies as substrates and signals in mammalian tissues. Physiol. Rev. *60*, 143–187.

Saha, S., Shalova, I.N., and Biswas, S.K. (2017). Metabolic regulation of macrophage phenotype and function. Immunol. Rev. *280*, 102–111.

Schoors, S., Bruning, U., Missiaen, R., Queiroz, K.C., Borgers, G., Elia, I., Zecchin, A., Cantelmo, A.R., Christen, S., Goveia, J., et al. (2015). Fatty acid carbon is essential for dNTP synthesis in endothelial cells. Nature *520*, 192–197.

Schugar, R.C., Huang, X., Moll, A.R., Brunt, E.M., and Crawford, P.A. (2013). Role of choline deficiency in the fatty liver phenotype of mice fed a low protein, very low carbohydrate ketogenic diet. PLoS One *8*, e74806.

Schugar, R.C., Moll, A.R., André d'Avignon, D., Weinheimer, C.J., Kovacs, A., and Crawford, P.A. (2014). Cardiomyocyte-specific deficiency of ketone body metabolism promotes accelerated pathological remodeling. Mol. Metab. *3*, 754–769.

Scott, C.L., Zheng, F., De Baetselier, P., Martens, L., Saeys, Y., De Prijck, S., Lippens, S., Abels, C., Schoonooghe, S., Raes, G., et al. (2016). Bone marrow-derived monocytes give rise to self-renewing and fully differentiated Kupffer cells. Nat. Commun. *7*, 10321.

Shi, X., Li, X., Li, D., Li, Y., Song, Y., Deng, Q., Wang, J., Zhang, Y., Ding, H., Yin, L., et al. (2014). β-Hydroxybutyrate activates the NF-kappaB signaling pathway to promote the expression of pro-inflammatory factors in calf hepatocytes. Cell Physiol. Biochem. *33*, 920–932.

Soufi, N., Hall, A.M., Chen, Z., Yoshino, J., Collier, S.L., Mathews, J.C., Brunt, E.M., Albert, C.J., Graham, M.J., Ford, D.A., and Finck, B.N. (2014). Inhibiting monoacylglycerol acyltransferase 1 ameliorates hepatic metabolic abnormalities but not inflammation and injury in mice. J. Biol. Chem. *289*, 30177–30188.

Trapnell, C., Roberts, A., Goff, L., Pertea, G., Kim, D., Kelley, D.R., Pimentel, H., Salzberg, S.L., Rinn, J.L., and Pachter, L. (2012). Differential gene and transcript expression analysis of RNA-seq experiments with TopHat and Cufflinks. Nat. Protoc. *7*, 562–578.

Vats, D., Mukundan, L., Odegaard, J.I., Zhang, L., Smith, K.L., Morel, C.R., Greaves, D.R., Murray, P.J., and Chawla, A. (2006). Oxidative metabolism and PGC-1β attenuate macrophage-mediated inflammation. Cell Metab. *4*, 13–24.

Verdeguer, F., and Aouadi, M. (2017). Macrophage heterogeneity and energy metabolism. Exp. Cell Res. *360*, 35–40.

Vogel, K.G., Paulsson, M., and Heinegard, D. (1984). Specific inhibition of type I and type II collagen fibrillogenesis by the small proteoglycan of tendon. Biochem. J. *223*, 587–597.

Wang, C., Wang, M., Zhou, Y., Dupree, J.L., and Han, X. (2014). Alterations in mouse brain lipidome after disruption of CST gene: a lipidomics study. Mol. Neurobiol. *50*, 88–96.

Wentz, A.E., d'Avignon, D.A., Weber, M.L., Cotter, D.G., Doherty, J.M., Kerns, R., Nagarajan, R., Reddy, N., Sambandam, N., and Crawford, P.A. (2010). Adaptation of myocardial substrate metabolism to a ketogenic nutrient environment. J. Biol. Chem. *285*, 24447–24456.

Wildenhoff, K.E., Johansen, J.P., Karstoft, H., Yde, H., and Sorensen, N.S. (1974). Diurnal variations in the concentrations of blood acetoacetate and 3-hydroxybutyrate. The ketone body peak around midnight and its relationship

to free fatty acids, glycerol, insulin, growth hormone and glucose in serum and plasma. Acta Med. Scand. *195*, 25–28.

Williamson, D.H., Lund, P., and Krebs, H.A. (1967). The redox state of free nicotinamide-adenine dinucleotide in the cytoplasm and mitochondria of rat liver. Biochem. J. *103*, 514–527.

Winberg, J., Kolset, S.O., Berg, E., and Uhlin-Hansen, L. (2000). Macrophages secrete matrix metalloproteinase 9 covalently linked to the core protein of chondroitin sulphate proteoglycans. J. Mol. Biol. *304*, 669–680.

Wishart, D.S., Jewison, T., Guo, A.C., Wilson, M., Knox, C., Liu, Y., Djoumbou, Y., Mandal, R., Aziat, F., Dong, E., et al. (2013). HMDB 3.0–the human metabolome database in 2013. Nucleic Acids Res. *41*, D801–D807.

Wong, B.W., Wang, X., Zecchin, A., Thienpont, B., Cornelissen, I., Kalucka, J., Garcia-Caballero, M., Missiaen, R., Huang, H., Bruning, U., et al. (2017). The role of fatty acid beta-oxidation in lymphangiogenesis. Nature *542*, 49–54.

Xu, J., Chi, F., Guo, T., Punj, V., Lee, W.N., French, S.W., and Tsukamoto, H. (2015). NOTCH reprograms mitochondrial metabolism for proinflammatory macrophage activation. J. Clin. Invest. *125*, 1579–1590.

Xu, J., and Kisseleva, T. (2015). Bone marrow-derived fibrocytes contribute to liver fibrosis. Exp. Biol. Med. (Maywood) *240*, 691–700.

Yamasaki, M., Hasegawa, S., Imai, M., Takahashi, N., and Fukui, T. (2016). High-fat diet-induced obesity stimulates ketone body utilization in osteoclasts of the mouse bone. Biochem. Biophys. Res. Commun. *473*, 654–661.

Yang, K., Cheng, H., Gross, R.W., and Han, X. (2009). Automated lipid identification and quantification by multidimensional mass spectrometry-based shotgun lipidomics. Anal. Chem. *81*, 4356–4368.

Youm, Y., Nguyen, K.Y., Grant, R.W., Goldberg, E.L., Bodogai, M., Kim, D., D'Agostino, D., Planavsky, N., Lupfer, C., Kanneganti, T.D., et al. (2015). The ketone metabolite β-hydroxybutyrate blocks NLRP3 inflammasome-mediated inflammatory disease. Nat. Med. *21*, 263–269.

STAR★METHODS

KEY RESOURCES TABLE

REAGENT or RESOURCE	SOURCE	IDENTIFIER
Antibodies		
Alexa Flour 488 conjugated goat anti-rabbit IgG	Invitrogen	#A11008; RRID: AB_143165
Alexa Fluor 647 conjugated donkey anti-goat IgG	Invitrogen	#A21447; RRID: AB_2535864
Polyclonal rabbit anti-BDH1	Proteintech Group	#15417-1-AP; RRID: AB_2274683
Rabbit anti-mHMGCS2	Santa Cruz Biotechnology	#SC-33828; RRID: AB_2118322
Rabbit polyclonal anti-SCOT	Proteintech Group	#12175-1-AP; RRID: AB_2157444
Goat anti-rabbit IgG conjugated to horseradish peroxidase	Southern Biotech	#4030-05; RRID: AB_2687483
Rabbit anti-actin	Sigma	#A2066; RRID: AB_476693
Chemicals, Peptides, and Recombinant Proteins		
2-Mercaptoethanol	Sigma	#M6250; #CAS 60-24-2
L-Citrulline	Sigma	#C7629; #CAS 372-75-8
L-Alanine	Sigma	#A7627; #CAS 56-41-7
Ethyl-acetoacetate	Sigma	#W241512; #CAS 141-97-9
Sodium D-βOHB	Sigma and Santa Cruz	#298360 and # sc-229050; #CAS 13613-65-5
[1,2,3,4-$^{13}C_4$] ethylacetoacetate	Cambridge Isotope Laboratories	#CLM-3297; Unlabeled CAS 141-97-9
Sodium D-[U-^{13}C]βOHB	Cambridge Isotope Laboratories	#CLM-3853; Unlabeled CAS 13613-65-5
[U-^{13}C]glucose	Cambridge Isotope Laboratories	#CLM-1396; Unlabeled CAS 50-99-7
T17:1 Triheptadecanoylglycerol (TAG)	Nu-Chekprep	#T-404
Luna NH_2 column (100 mm x 1 mm, 3 μm particle size)	Phenomenex	#00D-4377-A0
Ammonium acetate	Sigma	#73594-F; #CAS 631-61-8
Ammonium hydroxide	Honeywell	#44273-10x1mL; #CAS 1336-21-6
Methanol for LCMS	Fisher Scientific	#A456-4; #CAS 67-56-1
Acetonitrile for LCMS	Fisher Scientific	#A955-4; #CAS 75-05-8
Water for LCMS	Fisher Scientific	#W6-4; #CAS 7732-18-5
Lipopolysaccharide (LPS) from Escherichia coli O111:B4	Millipore	#L4391
Mouse recombinant interleukin-4 (IL-4)	PeproTech	#214-14
Carbonylcyanide-4-(trifluoromethoxy) phenylhydrazone (*FCCP*)	Enzo Life Sciences	#BML-CM120-0010; #CAS 370-86-5
HBSS	Invitrogen	#14175-095
RPMI 1640 Medium	Invitrogen	#11875-093
DMEM, high glucose	Invitrogen	#11965-092
Fetal bovine serum (FBS) HyClone	Fisher Scientific	#SH30087.03
Gibco L-Glutamine (200mM)	Fisher Scientific	#25030-081
Gibco Penicillin/streptomycin (10,000 U/mL)	Fisher Scientific	#15140122
Glucose- and serum-free DMEM	Invitrogen	#A14430-01
Protease inhibitor cocktail (cOmplete, mini, EDTA-free)	Sigma	#11836170001
Phosphatase inhibitor cocktail	Sigma	#524629
SuperScript II Reverse Transcriptase	Invitrogen	#100004925
SsoAdvanced Universal SYBR Green Supermix	Bio-Rad	#172-5274
Optimal Cutting Temperature (OCT) compound	Tissue-Tek	#4583

(*Continued on next page*)

Continued

REAGENT or RESOURCE	SOURCE	IDENTIFIER
4, 6-diamidino-2-phenylindole (DAPI)	Sigma	# D9542-5MG
Vectashield mounting medium with DAPI	Vector Laboratories	# H1200
E-Gel EX 2% agarose gel	Invitrogen	#G401002
Tamoxifen	Cayman Chemical	#13258; #CAS 10540-29-1
High fat diet	Research Diets	#D12492
Hepatic fibrogenic diet	Research Diets	#D09100301
Critical Commercial Assays		
BCA protein Assay kit	Thermo Fisher	#23225
RNeasy Mini Kit	Qiagen	#74016
RNeasy Lipid Tissue Mini Kit	Qiagen	#74804
RNase-Free DNase Set	Qiagen	#79256
Total ketone body (TKB) assay	Wako	#415-73301 and #411-73401
Autokit 3-HB (for βOHB)	Wako	#417-73501 and #413-73601
Glucose readers with glucose meter test strips	CVSHealth	N/A
QIAquick Gel Extraction Kit	Qiagen	#28506
TruSeq ChIP library systems	Illumina	#IP-202-1012
TruSeq RNA Library Preparation Kit	Illumina	#RS-122-2001
Deposited Data		
ChIP-seq data	GEO or (Czimmerer et al., 2018)	GEO: GSE106706
RNA-seq data	GEO or (Czimmerer et al., 2018)	GEO: GSE106706
Experimental Models: Cell Lines		
Primary macrophages isolated from C57BL/6NJ sub-strain hybrid mice carrying the *Oxct1*$^{flox/flox}$ allele or *Oxct1*$^{flox/flox}$ animals crossed with the ubiquitously expressed *Cre/ESR1* fusion [B6.Cg-Tg(CAG-cre/Esr1*)5Amc/J, stock number 004682, Jackson Laboratory]	(Cotter et al., 2013)	N/A
Experimental Models: Organisms/Strains		
Mouse: C57BL/6NJ sub-strain hybrid mice carrying the *Oxct1*$^{flox/flox}$ allele	(Cotter et al., 2013)	N/A
Mouse: *Oxct1*$^{flox/flox}$ animals crossed with the ubiquitously expressed *Cre/ESR1* fusion [B6.Cg-Tg(CAG-cre/Esr1*)5Amc/J, stock number 004682, Jackson Laboratory]	(Schugar et al., 2014)	N/A
Mouse: Oxct1$^{flox/flox}$ crossed with LysM-Cre strain from Jackson Laboratories (B6.129P2-Lyz2tm1(cre)ifo/J, stock number 004781, Jackson Laboratory)	N/A	N/A
Mouse: HMGCS2 knockdown	(Cotter et al., 2014)	N/A
Mouse: Stat6 KO	Jackson Laboratory	N/A
Mouse C57BL/6J	Jackson Laboratory	#000664
Oligonucleotides		
Hmgcs2-targeted ASO (5′-CTGTTTGTCACT GCTGGATG)	Ionis	#191229
Scrambled sequence control ASO (5′-CCTTCC CTGAAGGTTCCTCC)	Ionis	#141923
Software and Algorithms		
MSConvert free open source	http://proteowizard.sourceforge.net/tools.shtml	N/A
XCMSOnline requires registration, free open source	https://xcmsonline.scripps.edu/landing_page.php?pgcontent=institute	RRID: SCR_015538

(*Continued on next page*)

Continued

REAGENT or RESOURCE	SOURCE	IDENTIFIER
Metlin database requires registration, free open source	https://metlin.scripps.edu/landing_page.php?pgcontent=mainPage	RRID: SCR_010500
R package free open source	http://r-pkgs.had.co.nz/	N/A
R studio (Ver 1.0.153) free open source license	https://www.rstudio.com/products/rstudio/download/	N/A
X13CMS (v.1.4) package free open source license	http://pattilab.wustl.edu/software/x13cms/x13cms.php	N/A
Compound Discoverer (ver. 2.1)	Thermo	N/A
Xcalibur	Thermo	RRID: SCR_014593
PIUMet	http://fraenkel-nsf.csbi.mit.edu/PIUMet/	N/A
MBRole 2.0	http://csbg.cnb.csic.es/mbrole2/	RRID: SCR_014684
GraphPad (ver 7.03)	GraphPad software	RRID: SCR_002798
ImageJ free open source license	NIH	RRID: SCR_003070
KEGG database	https://www.genome.jp/kegg/	RRID: SCR_012773
BioCyc database	https://biocyc.org/	RRID: SCR_002298
Quantity One software	BioRad	RRID: SCR_014280
TopHat	http://cole-trapnell-lab.github.io/projects/tophat/	RRID: SCR_013035
Cufflinks	http://cole-trapnell-lab.github.io/projects/cufflinks/	RRID: SCR_014597

CONTACT FOR REAGENT AND RESOURCE SHARING

Further information and requests for resources and reagents should be directed to and will be fulfilled by the Lead Contact, Peter Crawford (crawforp@umn.edu).

EXPERIMENTAL MODEL AND SUBJECT DETAILS

Animal Models and Animal Model for Primary Cells

Primary macrophage cultures were obtained from 9- to 16-week old male and female C57BL/6NJ sub-strain hybrid mice carrying the *Oxct1*$^{flox/flox}$ allele previously described (Cotter et al., 2013). This allele encodes SCOT and is functionally wild type with no obvious phenotype in carriers. Germline ubiquitous SCOT-KO mice are fully lethal in the neonatal period. To generate adult whole-body SCOT knockout mice, *Oxct1*$^{flox/flox}$ animals were crossed with the ubiquitously expressed *Cre/ESR1* fusion [B6.Cg-Tg(CAG-cre/Esr1*)5Amc/J, stock number 004682, Jackson Laboratory], and 6-week old Cre-positive offspring and their Cre-negative littermate controls were subjected to a 17-day tamoxifen (Cayman Chemical) injection regimen at 20 mg/kg animal weight. A two-week washout period after the final injection was allowed for pre-existing SCOT protein turnover (Schugar et al., 2014). These animals are designated as 'SCOT-KO' and 'WT', respectively, where they were used in the experiments described below. Successful KO was confirmed via Western blot for SCOT protein in heart and skeletal muscle and via lack of [^{13}C]AcAc oxidation in bone marrow-derived macrophages (BMDM).

Macrophage specific SCOT-KO mice were generated by successive rounds of breeding of Oxct1$^{flox/flox}$ mice to the LysM-Cre strain from Jackson Laboratories (B6.129P2-Lyz2tm1(cre)ifo/J, stock number 004781, Jackson). Genotyping primers can be found in Table S5.

To create HMGCS2 knockdown mice, ASO treatment was initiated in six week-old mice by injecting (25 mg/kg) of Hmgcs2-targeted ASO (Ionis 191229; 5′-CTGTTTGTCACTGCTGGATG) or scrambled sequence control ASOs (Ionis 141923; 5′-CCTTCCCTGAAGGTTCCTCC) biweekly for 4 weeks prior to initiation of high fat diet, and were continued through high fat diet administration.

To study the role of exogenously-delivered ketone bodies in liver fibrosis, 7 week-old male C57BL/6J mice (stock number 000664) were purchased from Jackson Laboratories.

Mice were maintained on a standard low-fat chow diet (2016 Teklad global 16% protein rodent diet), 8 weeks on high fat diet (D12492; Research Diets; 60% kcal fat, 20% protein, 20% carbohydrate) or 4 weeks on a hepatic fibrogenic diet [D09100301; Research Diets: 40% kcal fat, predominantly *trans* fat (*trans* oleic and *trans* linoleic acids), 20% kcal fructose (total carbohydrate, 40% kcal), and cholesterol (2% w/w)], and given autoclaved water ad libitum. Lights were off between 1900 and 0700 in a room maintained at 22°C. All animal experiments were performed through protocols formally approved by the Institutional Animal Care and Use Committees at Sanford Burnham Prebys Medical Discovery Institute-Lake Nona and the University of Minnesota.

Bone Marrow- Derived Macrophage (BMDM) Isolation and Culture

Animals were sacrificed by cervical dislocation prior to harvest of the femurs and tibia of both legs. The marrow was flushed out using cold Ca^{2+} and Mg^{2+}-free Hank's buffered salt solution (HBSS) delivered through 3-mL syringes and 23- to 27-guage needles, respectively. The pooled marrow from one animal was dispersed using a P1000 micropipette, and debris was allowed to settle before the suspension was transferred into fresh tubes and centrifuged. The resulting pellet was resuspended in BMDM differentiation media (RPMI (Thermo Fisher, includes 10 mM glucose) with 10% L929 conditioned media, 10% fetal bovine serum (FBS), 2 mM glutamine, 10 U/mL penicillin/streptomycin) and distributed into tissue culture plates at an average density of one animal into 100-cm^2 total surface area for growth. Fresh differentiation media was added two days after isolation. At day 4, exhausted media and non-adherent cells were aspirated from the plates, cells were washed with pre-warmed HBSS, and fresh media was added. After a second media change on day 6, mature macrophages were used on day 7 for labeling and treatment studies. L929 conditioned media was generated by culturing L929 cells to confluence over the course of 4-5 days in 10% FBS supplemented DMEM (50 mL per 175 cm^2 flask), after which the media was removed, filtered, and aliquoted for frozen storage. In all studies, cells isolated from a single animal were counted as a single replicate unless otherwise indicated.

METHOD DETAILS

Synthesis of AcAc

AcAc was synthetized by a base-catalyzed hydrolysis of ethylacetoacetate (ethyl-AcAc): 8 mL of 1 M NaOH was added to 1 mL ethyl-AcAc while stirring at 60°C. After 30 min, the reaction was neutralized with 50% HCl to pH 8, and the concentration of AcAc was determined with a colorimetric enzyme-based total ketone body (TKB) assay (Wako) prior to aliquoting and storage at -80°C.

Exogenous Delivery of Ketone Bodies

To study the role of exogenously-delivered ketone bodies in liver fibrosis, 7 week-old male C57BL/6J mice were acclimatized for one week, and then maintained on fibrogenic diet for 4 weeks and injected twice daily i.p. (10 μmol/g body weight) with AcAc, D-βOHB or their vehicles. Because the AcAc synthesis reaction generates equimolar quantities of ethanol and AcAc and no further purification of AcAc was undertaken, ethanol was used as a vehicle for AcAc injections: 250 μL i.p. equimolar (=∼5%) ethanol. Sodium D-βOHB (Santa Cruz, pH corrected to 7.0, 250 μL i.p.), and equimolar NaCl was used as a vehicle control for D-βOHB mice (250 μL). C57BL/6J mice were used for the exogenous ketone (compared to vehicle control) mice fed fibrogenic diet fed for four weeks, receiving injections every 12 h.

Labeling of Cultured Primary Cells by Stable Isotopes

BMDMs were incubated in glucose- and serum-free DMEM containing 2 mM glutamine for 1 h prior to the introduction of ^{13}C-labeled substrates (Cambridge Isotope Laboratories). Uniformly labeled sodium D-[U-^{13}C]βOHB (1 mM), or [U-^{13}C]AcAc (1 mM) were added to DMEM containing 10 mM glucose and 2 mM glutamine. For experiments using exogenously added [U-^{13}C]glucose (10 mM), glucose-free DMEM was used. Uniformly labeled AcAc was generated by a base-catalyzed hydrolysis of [1,2,3,4-$^{13}C_4$] ethylacetoacetate using same protocol as for unlabeled AcAc. EtOH was added to control experiments at a concentration equal to that of the highest amount of AcAc used due to the equimolar quantity of EtOH in the sample after AcAc synthesis. Labeling experiments were done for 6h and/or 24h, at which points the media was removed and cells were processed using the metabolite extraction method described below. To induce M1 or M2 polarization in BMDMs, lipopolysaccharide (LPS, Millipore) or IL-4 (PeproTech), respectively, were added to a final concentration of 25 ng/mL to the labeling media at the same time the media was introduced to the cells after their 1 h incubation in glucose- and serum-free DMEM. All drug (carbonyl cyanide-4-(trifluoromethoxy)phenylhydrazone (FCCP, Enzo Life Sciences) and substrate treatments (AcAc) were introduced simultaneously, with the labeling media, macrophage polarizing agents, and maintained for either 6 h or 24 h.

Extraction of Metabolites from Cells, Liver Tissue and Conditioned Media

Cells, liver tissues and conditioned media were extracted using previously described method (Chen et al., 2016) with modifications. *Cells* were washed twice with pre-warmed PBS and once with Milli-Q water. The tissue culture plate was then placed in a liquid nitrogen bath for 30 s to quench metabolism and initiate cell lysis. Cold MeOH (-20°C) was added at a ratio of 500 μL per 6-cm dish or single well of a 6-well plate, the cells were scraped, transferred to 1.7 mL polypropylene microfuge tubes, and MeOH was evaporated using a Speed-Vac (Savant SPD 1010). Frozen lobes of liver *tissue* were lyophilized prior to extraction. ***Cells***, and lyophilized ***liver tissue*** were extracted using cold (-20°C) 1000 μL of 2:2:1 MeOH:acetonitrile:H_2O. ***Conditioned media*** (200 μL) was extracted with cold (-20°C) 800 μL of 1:1 MeOH:acetonitrile (ACN). Thereafter, all samples were extracted by three cycles of vortexing, freeze-thawing, and water bath sonication. The samples were then incubated at -20°C for 1 h followed by a 10 min spin at maximum speed to remove proteins from the solvent, which was then transferred to fresh tubes and evaporated off in the speed-vac. The dried metabolite pellet was reconstituted in 40 μL (cells) or 100 μL (liver tissue or conditioned media) 1:1 acetonitrile:H_2O with the aid of vortexing and sonication, and incubated at 4°C for 1 h. Samples were then spun down and the supernatant was analyzed by LC/MS.

Targeted and Untargeted LC/MS Analysis

Liquid chromatography was performed on a Dionex Ultimate 3000 RSLC using a Phenomenex Luna NH_2 column (100 mm x 1 mm, 3 μm particle size) for untargeted metabolomics surveys. We used hydrophilic interaction liquid chromatography (HILIC) mode, with the following mobile phase compositions: A = 95% H_2O, 5% ACN, 10 mM NH_4OAc/ NH_4OH, pH 9.5; B = 95% ACN, 5% H_2O, 10 mM NH_4OAc/ NH_4OH, pH 9.5. Unless otherwise stated, the extracts were usually separated using binary gradient 75-0% B for 45 min, then 0% B for 12 min, and 75%B for 13 min at 50 μL/min. [^{13}C]glucose analysis of SCOT WT and SCOT KO IL-4 polarized BMDMs, and tissue extract analysis were performed with an extended gradient starting at 100% B for 5 min, 100-0% of B for 45 min, 0-100% of B for 7 min, and 100% B for next 13 min. Column temperature was maintained at 30°C, and injection volume was 4 μL. Citrulline quantification in conditioned media was performed using isocratic elution of 75% B for 6 min; flow rate 50 μL/min; column temperature at 30°C; and injection volume 4 μL. Prior to the analysis, to the conditioned media, 15 μM alanine was added as an internal standard. Mass spectrometry (MS) was performed on a Thermo Q Exactive Plus with heated ESI source. The MS was operated mostly in negative mode with exception of citrulline analysis where positive mode was applied. MS resolution was set to 70,000 and the AGC target to $3e^6$ ions with a maximum injection time of 200 ms. The mass scan range for extract analysis was 68-1020 *m/z*, while for citrulline, 80-200 *m/z*. In targeted analysis, full scan mode was used with the addition of an inclusion list of the ions of interests. The resolution was set to 35,000, AGC target to $2e^5$ ions with a maximum injection time of 100 ms, isolation width 2.0 *m/z,* and fixed normalized collision energy 35 (arbitrary unit). Common ESI parameters were: auxiliary gas 10, sweep gas 1, spray voltage -3 kV, capillary temperature 275°C, S-lens RF 50, and auxiliary gas temperature 150°C. The sheath gas flow for extract analysis was set to 35 (arbitrary unit).

LC/MS Data Processing

Data from liver metabolomics and stable isotope tracing untargeted metabolomics (ITUM) experiments (.RAW files) were converted to mzXML format using MSConvert with the vendor peak-picking option selected, and processed using XCMSonline or X^{13}CMS R package as described previously (Cotter et al., 2014; Huang et al., 2014; Mahieu et al., 2016a, 2016b). The .RAW data files were uploaded for analysis using Compound Discoverer (ver. 2.1). Liver metabolomics data were uploaded to ***XCMSonline***, and analyzed based on the method ''HPLC / Orbitrap - HPLC with ~60 min gradient / Orbitrap'' available online with modifications. The feature detection parameters were 5 ppm, peak width interval to 10-180 min, integration method to 2, and prefilter intensity to 500. Retention time correction was changed to 0.5 prof Step (in *m/z*), while alignment bw to 30 and mzwid to 0.025. Peaks with fold change greater than 2 were selected, with median fold change normalization option. For ***Compound Discoverer 2.1.***, analysis was performed based on the ''untarg. Metabolomics w Statistics Detect Unknowns w Mapped Pathways and ID using online databases'' workflow with modifications. To select the spectra, 60-1500 Da *m/z* scan was used with intensity threshold 500, and highest charge 4. We applied adaptive alignment curve method with maximum 4 min RT shift and 5 ppm mass tolerance. Unknown compounds were detected with 5 ppm mass tolerance, and grouped with 1 min RT tolerance. Maximum of 10 compounds per feature were predicted and searched against ChemSpider and KEGG database with 5 ppm mass tolerance. For ***ITUM X^{13}CMS*** base analysis, the data was processed using R studio where the XCMS (v. 1.4) package was used to pick chromatographic (method = 'centWave', ppm = 2.5, peakwidth = c(20, 180)) peaks and align retention time (bw=10, mzwid=0.015, retention time correction method = 'obiwarp') across samples within an experiment. X^{13}CMS (v.1.4) was used on the output to extract isotopologue groups. The parameters used for X^{13}CMS are RTwindow = 10, ppm = 5, noiseCutoff = 10000, intChoice = ''intb'', alpha = 0.05 within getIsoLabelReport().

Identification of Metabolites Detected in LC/MS and Pathway Analysis

The identity of a subset of metabolites was confirmed by matching the retention time and MS/MS of standard compounds run using identical chromatographic separation conditions (Table S5). Another subset was assigned putative identifications based on (i) match of unlabeled accurate masses in the Metlin database, (ii) molecular formulas and structures, which could produce the observed number of carbon labels in a biological context, and (iii) predicted retention time based on chemical similarity to standard compounds (Table S5). Pathway analysis was performed with the aid of PIUMet analysis (Pirhaji et al., 2016) and MBRole web-based application (Lopez-Ibanez et al., 2016). For PIUMet analysis the files containing input *m/z* values, polarization modes, and –log of p values were uploaded for the analysis. For labeled compound found just in one macrophage polarization state, the p value was assumed to be 0.05. For MBRole analysis, the putative identification were assigned based on the hmdb.ca (Wishart et al., 2013) database search from PIUMet output. HMDB output was mapped using MBRole against mouse KEGG or BioCyc database.

Gene Expression Analysis

RNA was purified from whole liver or inguinal subcutaneous fat lysates homogenized in RLT Buffer (Qiagen) with 1% of 2-Mercaptoethanol or from cell extracts using the RNeasy Mini Kit (Qiagen) or RNeasy Lipid Tissue Mini Kit (Qiagen) following the manufacturer's guidelines. Reverse transcripts were generated using SuperScript II (Invitrogen), while real-time reverse-transcription polymerase chain reaction (RT-PCR) was performed using SsoAdvanced Universal SYBR Green Supermix (Bio-Rad) on the CFX384 Real-Time System (Bio-Rad). Transcripts were quantified using the $2^{-\Delta\Delta Ct}$ method, with *Rpl32* as an internal reference. Primer sequences are listed in Table S5.

Immunoblotting

Protein extracts were collected from 6-well macrophage cultures by scraping in protein lysis buffer (PLB) containing 20 mM Tris-HCl, 150 mM NaCl, 1 mM EDTA, 1% Triton-X 100 at pH 7.5 and supplemented with protease inhibitor cocktail (cOmplete, mini, EDTA-free, Roche) and phosphatase inhibitor cocktail (Sigma). Whole liver protein lysates were prepared from frozen tissue sections and homogenized in ten times volume (microliters) to mass in PLB with inhibitors. Immunoblot analysis was performed as described previously (Wentz et al., 2010). Protein targets of interest were probed with the following primary antibodies: polyclonal rabbit anti-BDH1 (Proteintech Group; 1:1200); polyclonal rabbit anti-SCOT (Proteintech Group; 1:5000), rabbit anti-mHMGCS2 (Santa Cruz Biotechnology; 1:2000). Secondary antibodies conjugated to horseradish peroxidase was goat anti-rabbit IgG (Southern Biotech; 1:2000 for BDH1; 1:15000 for SCOT; 1:50000 for HMHCS2). All targets were normalized to actin, which was probed with a polyclonal rabbit anti-actin (Sigma; varying dilutions) and goat anti-rabbit IgG-HRP (Southern Biotech). Band intensities were measured densitometrically using Quantity One software (Bio-Rad).

Histology and Immunohistochemical Staining

Following sacrifice, mouse liver sections were either fixed in 10% neutral buffered formalin (VWR International) or cryo-preserved in Optimal Cutting Temperature (OCT) compound (Tissue-Tek). Formalin tissues were embedded in paraffin, sectioned via microtome, and stained with hematoxylin and eosin, PicroSirius Red (Sanford Burnham Prebys Histology and University of Minnesota CTSI Histology Cores), or Oil Red O. Bright field hematoxylin and eosin and Oil Red O images were obtained using the EVOS XL Core Cell Imaging System (Life Technologies), polarized-light PicroSirius Red images were acquired using the Eclipse LV100N POL (Nikon) or Leica DFC7000T (Leica). PicroSirius Red was quantified using ImageJ software, followed by averaging the percent area of fibrosis for 20 randomly selected fields at 20x magnification. To selectively quantify sinusoidal fibrosis and exclude collagen juxtaposed to luminal openings of the central vasculature, central veins and portal triads were excluded from the quantification. Frozen tissue sections preserved in OCT were cut in 10 μm slices using the Leica 1900 UV Cryostat at -20°C. Tissue sections were fixed on slides using 2% paraformaldehyde for 1 h, depermeabilized for 20 min in 0.25% Triton X-100 (Tx-100), and blocked in 5% BSA/PBS-0.1% Tx-100 1 h. Immunostaining for F4/80-positive cells was performed as previously described (Schugar et al., 2013). Rabbit polyclonal anti-SCOT (Proteintech Group; 1:150) was incubated for 1 h at room temperature, followed by Alexa Flour 488 conjugated goat anti-rabbit IgG (Invitrogen) for 30 min, and counterstained with 4, 6-diamidino-2-phenylindole (DAPI; 1:10,000 in 1x PBS/0.1% Tx-100) for 5 min. Goat polyclonal anti-desmin (R&D Systems; 1:40) was incubated overnight at 4°C, followed by Alexa Fluor 647 conjugated donkey anti-goat IgG (Invitrogen) for 2 h at room temperature and mounted with Vectashield mounting medium with DAPI (Vector Laboratories). Primary and secondary antibodies were prepared in 5% BSA/1x PBS/0.1% Tx-100. All immunofluorescent images were captured using a Nikon A1R VAAS Inverted Confocal Microscope at 40x magnification for images included in the results, and quantifications were at 20x magnification. The number of $F4/80^{+}$ macrophages per mm^2 depicts the average number in 20 acquired images.

RNA-Seq and Analysis

RNA-Seq library was prepared from two biological replicates by using TruSeq RNA Sample Preparation Kit (Illumina) according to the manufacturer's protocol. Briefly, 2.5 μg total RNA was used for the library preparation. In the first step poly-A tailed RNA molecules (mRNA) were purified with poly-T oligo-attached magnetic beads. Following the purification, mRNA is fragmented using divalent cations at 85°C, then first strand cDNA was generated using random primers and SuperScript II reverse transcriptase (Invitrogen). This was followed by the second strand cDNA synthesis, then double stranded cDNA fragments went through an end repair process, the addition of a single 'A' base and then barcode indexed adapter ligation. Adapter-ligated products were enriched with adapter specific PCR to create cDNA library. Agarose gel electrophoresis was performed on E-Gel EX 2% agarose gel (Invitrogen) and the library was purified from the gel using QIAquick Gel Extraction Kit (Qiagen). Fragment size and molar concentration were checked on Agilent BioAnalyzer using DNA1000 chip (Agilent Technologies). Libraries were sequenced with Illumina HiScanSQ sequencer. The TopHat-Cufflinks-CummeRbund toolkit trio (Trapnell et al., 2012) was used for mapping spliced reads, making transcript assemblies, and getting, sorting and visualizing gene expression data. Expressional values were in FPKM format: Fragments Per Kilobase of exon per Million fragments mapped. Data are available under the following accession number: GEO: GSE106706.

ChIP-Seq (Chromatin Immunoprecipitation Followed by Sequencing) and Analysis

ChIP was performed as previously described (Daniel et al., 2014a, 2014b). Libraries were prepared with TruSeq ChIP library systems (Illumina) according to the manufacturer's instructions. Fragment distribution of libraries was assessed with Agilent Bioanalyzer and libraries were sequenced on a HiSeq 2500 platform. The primary analysis of ChIP-seq derived raw sequence reads has been carried out using our ChIP-seq analysis command line pipeline (Barta, 2011). Data is available under the following accession number: GEO: GSE106706.

Shotgun Lipidomics-Guided TAG Quantification

Frozen liver samples were weighed (20-30 mg) and homogenized in ice cold water (Han et al., 2004). According to the BCA protein concentration result, an appropriate amount of internal standard (T17:1 Triheptadecanoylglycerol from Nu-Chekprep, USA) was added to the homogenate. Approximately 130 μL of homogenate with internal standard was extracted using previously described methods (Wang et al., 2014), dried under nitrogen, diluted to a final concentration of ~500 fmol/μL and infused directly to TSQ

Vantage triple quadrupole mass spectrometer (Thermo Fisher). Shotgun lipidomics was performed according to published method (Yang et al., 2009) where acyl chains were identified by neutral loss scan of $[TAG+Li]^+$ adducts at -35 eV collision energy and quantified using an in house algorithm.

Serum Ketone Body, Glucose Assays and Glucose Tolerance Test (GTT)

Serum total ketone body (TKB), βOHB (Autokit 3-HB) (Wako) and glucose assays were performed according to manufactures protocols. GTT test was performed as described previously (Garbow et al., 2011).

QUANTIFICATION AND STATISTICAL ANALYSIS

Data were plotted and statistical analysis was performed on Prism (GraphPad) v7.0. Numbers of observations, assessments of normal distributions, and statistical tests applied are provided in the Figure Legends. When possible, investigators were blinded to the genotype of mice.

DATA AND SOFTWARE AVAILABILITY

All data obtained from X13CMS and XCMSonline analysis are available in Supplemental Tables of this manuscript. Chip-seq and RNA-seq data are available under the following accession number: GEO: GSE106706 or in Czimmerer et al. (2018). Most of utilized software platforms used in this manuscript were free open source licenses.